Laminar and turbulent flows over hydrophobic surfaces with shear-dependent slip length

Sohrab Khosh Aghdam and Pierre Ricco*
Department of Mechanical Engineering, The University of Sheffield, Mappin Street, S1 3JD Sheffield, United Kingdom

2016 Khosh, S.K. Ricco, P. Laminar and turbulent flows over hydrophobic surfaces with shear-dependent slip length, Phys. Fluids, 28, 035109.

Motivated by extensive discussion in the literature, by experimental evidence and by recent direct numerical simulations, we study flows over hydrophobic surfaces with shear-dependent slip lengths and we report their drag-reduction properties. The laminar channel-flow and pipe-flow solutions are derived and the effects of hydrophobicity are quantified by the decrease of the streamwise pressure gradient for constant mass flow rate and by the increase of the mass flow rate for constant streamwise pressure gradient. The nonlinear Lyapunov stability analysis, first applied to a two-dimensional channel flow by A. Balogh, W. Liu, and M. Krstic ["Stability enhancement by boundary control in 2-D channel flow" *IEEE Trans. Autom. Control*, 2001, vol. 46, pp. 1696-1711], is employed on the three-dimensional channel flow with walls featuring shear-dependent slip lengths. The feedback law extracted through the stability analysis is recognized for the first time to coincide with the slip-length model used to represent the hydrophobic surfaces, thereby providing a precise physical interpretation for the feedback law advanced by Balogh *et al.* (2001). The theoretical framework by K. Fukagata, N. Kasagi, and P. Koumoutsakos ["A theoretical prediction of friction drag reduction in turbulent flow by superhydrophobic surfaces" *Phys. Fluids*, 2006, vol. 18, 051703] is employed to model the drag-reduction effect engendered by the shear-dependent slip-length surfaces and the theoretical drag-reduction values are in very good agreement with our direct numerical simulation data. The turbulent drag reduction is measured as a function of the hydrophobic-surface parameters and is found to be a function of the time- and space-averaged slip length, irrespectively of the local and instantaneous slip behaviour at the wall. For slip parameters and flow conditions that could be realized in the laboratory, the maximum computed turbulent drag reduction is 50% and the drag reduction effect degrades when slip along the spanwise direction is considered. The power spent by the turbulent flow on the hydrophobic walls is computed for the first time and is found to be a non-negligible portion of the power saved through drag reduction, thereby recognizing the hydrophobic surfaces as a passive-absorbing drag-reduction method. The turbulent flow is further investigated through flow visualizations and statistics of the relevant quantities, such as vorticity and strain rates. When rescaled in drag-reduction viscous units, the streamwise vortices over the hydrophobic surface are strongly altered, while the low-speed streaks maintain their characteristic spanwise spacing. We finally show that the reduction of vortex stretching and enstrophy production is primarily caused by the eigenvectors of the strain rate tensor orienting perpendicularly to the vorticity vector.

I. INTRODUCTION

Turbulence is one of the most challenging problems in classical physics and has been studied for more than a century with the aim to understand its underlying principles. A key area of turbulence research has been flow control, i.e., the development of methods that modify the flow to achieve a beneficial effect, such as the attenuation of turbulent kinetic energy to obtain drag reduction [1].

Our research interest is on hydrophobic surfaces, whose main characteristic is a finite effective slip velocity at the wall [2]. These surfaces may achieve drag reduction for both laminar and turbulent flows [3, 4], delay the transition to turbulence [5], and operate over a wide range of Reynolds numbers relevant for technological applications, such as flows over marine vessels [6]. In particular, we are motivated by recent experimental and numerical research works that suggest that the characteristic slip length of the wall velocity may be a function of the wall-shear stress [4, 7–9]. The crucial observation is that this dependence is likely to be true especially for liquids in the turbulent regime flowing past hydrophobic surfaces because these flows exert shear stresses that are much larger than in the laminar regime.

Most of hydrophobic surfaces feature alternating patches of solid wall and trapped air pockets. The interaction between the viscous flow and the air pockets gives rise to the drag reduction effect. The inspiration for their design

* Email:p.ricco@sheffield.ac.uk

comes from the water-repellent lotus leaves [10]. More recently, liquid-infused rigid porous surfaces, the so-called Slippery Liquid-Infused Porous Surfaces (SLIPS) [11, 12] mimicking the features of the nepenthes pitcher plant, have shown very interesting hydrophobic, anti-biofouling and self-cleaning properties. Drag reduction over SLIPS has been reported in laminar [13, 14] and turbulent regimes [15].

A. Laminar and transitional flows over hydrophobic surfaces

The remarkable hydrophobic properties of these surfaces have spurred scientists to investigate their effect on laminar flows with the aim of reducing the friction drag [7, 16, 17]. One of the first experimental works of a laminar flow over superhydrophobic surfaces showed that 14% drag reduction could be attained [3], while Ou *et al.* [18] reported a 40% drag reduction.

The effect of hydrophobic surfaces has mainly been modelled in two ways. In the first model, which traces back to Navier [19], the fluid obtains a finite slip velocity at the boundary and a linear relation between the local wall velocity and the shear-rate has been assumed to exist, i.e., $u_{\mathrm{wall}} = b\, \partial u/\partial y|_{\mathrm{wall}}$, where the constant b is called the slip length. The second model distinguishes between the interaction of the liquid with the solid portions of the wall, modelled by the standard no-slip condition, and the dynamics between the liquid and the trapped air pockets, often modelled simply through a shear-free boundary. Philip [2] used the second framework and extracted analytical solutions for the laminar Poiseuille pipe flow. Lauga and Stone [7] extended Philip [2]'s work to the pipe-flow case with different orientation of the micro-patterns and correlated these analytical results with the effective slip length for the first time.

The research works on stability and transition to turbulence are more limited. The most notable effort is by Min and Kim [5], who demonstrated numerically that the critical channel-flow Reynolds number for linear stability increases when the walls are hydrophobic and that the laminar-turbulent transition can be significantly delayed.

B. Turbulent flows over hydrophobic surfaces

Inspired by the success of hydrophobic surfaces to reduce laminar drag, research efforts were soon directed toward turbulent drag reduction. Daniello *et al.* [20] proved experimentally that turbulent drag reduction as high as 50% can be obtained with hydrophobic surfaces. Drag reduction experiments in free-stream transitional and turbulent boundary layer flows over flat surfaces sprayed with hydrophobic nanoparticles were carried out by Aljallis *et al.* [21]. A crucial observation was the eventual depletion of the surface at high-shear rates and the subsequent drag increase. The experimental work by Bidkar *et al.* [22] showed that sustained turbulent drag reduction of up to 30% can be achieved over random-textured hydrophobic surfaces. Turbulent drag reduction of 14% over the SLIPS has been measured experimentally by Rosenberg *et al.* [15].

In the direct numerical simulations (DNS) by Min and Kim [4], the hydrophobic surface was implemented through Navier [19]'s model, thereby enforcing an effective slip length. Maximum drag reduction occurred for slip in the streamwise direction only, while slip along the spanwise direction was detrimental for drag reduction. Min and Kim [4]'s parametric study on the influence of slip lengths was extended in the DNS work of Busse and Sandham [9]. In a later work, Hasegawa *et al.* [23] numerically studied a turbulent channel flow with streamwise-varying micro-grooves. The boundary conditions were expressed through a mobility tensor, relating the slip velocity and the wall-shear stress, in line with other works on flows over anisotropic hydrophobic patterns [24, 25].

The DNS by Martell *et al.* [26] modelled a superhydrophobic surface through periodically patterned micro-cavities filled with trapped air, confirming most of the experimental findings by Daniello *et al.* [20]. Martell *et al.* [27] numerically simulated flows at three Reynolds numbers, demonstrating that, even though the Reynolds number changed, the same drag reduction is obtained as long as the scales of the wall texture are the same in wall units. Martell *et al.* [27] and Lee *et al.* [28] both proved that the drag reduction performance improves as the bulk Reynolds number increases if the texture scales are kept constant when scaled in outer units.

Fukagata *et al.* [6] proposed a theoretical formula that analytically predicts the dependence of drag reduction on the slip length and the Reynolds number. They showed that increasing the Reynolds number leads to a weak decrease of the drag-reducing effect when slip is along the streamwise direction only. This negligible effect was also reported by Busse and Sandham [9]. Further discussion on the physics of turbulent drag reduction by hydrophobic surfaces can be found in Rothstein [29] and in the more recent DNS works by Jelly *et al.* [30] and Lee *et al.* [28], who reported the changes of turbulent kinetic energy balance, in particular the strengthening of the energy production near the slip patches and a detailed study of secondary and tertiary flows induced by the wall texture.

C. Motivation behind the study of hydrophobic surfaces featuring shear-dependent slip length

In this paper, for the first time theoretical and numerical results of laminar and turbulent flows bounded by hydrophobic walls exhibiting shear-dependent slip lengths are presented. We have been motivated by several discussions in experimental articles [31–34] and numerical articles [4, 7, 9, 35], from which it emerges that a shear-dependent slip length is likely to occur especially in the turbulent regime as the wall-shear stress can reach high values. Churaev *et al.* [33] first experimentally reported slip lengths increasing with the shear rate. Lauga and Stone [7] point out that the high wall shear may stretch the air pockets, thereby increasing the portion of the wall surface covered by air and causing the effective slip length to depend on the shear stress. Choi and Kim [8] show that, in both water and mixed water-glycerin flows, the slip length depends on the wall shear, although they state that this effect may be influenced by viscous heating at high shear rates. Shear-dependent slip lengths were also shown by Choi *et al.* [32] at smaller scales. Although the linear Navier's model was used by Min and Kim [4], they remark that experimental works show that the slip length in general depends on the shear rate. Busse and Sandham [9] further advocate that future research ought to consider this dependence to improve the modelling of hydrophobic surfaces under high-shear turbulent flows. Schönecker *et al.* [35] point out that the hydrophobic slip depends on the dynamics of the enclosed gas and that the gas viscosity impacts on the slip length, implying that the latter depends on the shear rate. In the laminar case, steps in this direction have been taken by Schönecker and Hardt [36], who computed a streamwise-dependent slip length for flows over rectangular air-filled cavities. More recently, the direct numerical simulation study by Jung *et al.* [37] of a turbulent flow over thin air layers showed that in high-drag-reduction cases the computed slip length may depend on the shear at the water-air interface.

Furthermore, the SLIPS hydrophobic surfaces [11, 12], studied for the first time below a turbulent flow by Rosenberg *et al.* [15], may also exhibit shear-dependent slip lengths. The liquid trapped in the porous substrate is usually a Newtonian oil, but non-Newtonian liquids could also be a sensible choice because they would stick well to the porous rigid substrate, an essential requirement for these textures to function properly. It is therefore likely that the interaction between the flowing water and the trapped oil would be characterized by shear-dependent slip lengths. Schönecker and Hardt [38] further remark that the viscosity of the trapped oil in the SLIPS, and consequently the shear at the liquid-oil interface, must be considered to model these surfaces. Furthermore, when representing the SLIPS by the slip-length model, the issue of capturing accurately the near-wall spatially inhomogeneous interaction with the air-pockets pattern is avoided because the liquid infusing the substrate is uniformly distributed below the flowing liquid.

As a first study on laminar and turbulent flows over hydrophobic surfaces which show wall-slip properties that depend on the wall-shear stress, we have chosen to extend the slip-length model employed by Min and Kim [4] and Busse and Sandham [9]. This approach clearly implies that, when representing surfaces with trapped air pockets, the precise texture features are not modelled and that the characteristic lengths of the hydrophobic surface are smaller than the near-wall viscous scales of the turbulence. The other option to model these surfaces would have been to resolve the complex interaction between the turbulent flows and the textured patterns of alternating patches of solid surfaces and air pockets. The modelling of the slip/no-slip pattern would have been more realistic, but, in order to synthesize the dependence of the wall slip on the wall shear, the widely-adopted boundary conditions of zero velocity over the solid wall and of zero shear over the air pockets would not have been adequate because the corresponding effective slip length would not have been shear dependent. This approach would have required the precise characterization of the interaction between the liquid flow and the gas, i.e., the resolution of the flow dynamics of the air motion in the pockets, as amply discussed by Schönecker *et al.* [35].

D. Objectives of the present work

A linear dependence between the slip length and the wall shear has been chosen, motivated by the experimental findings by Churaev *et al.* [33] and Choi and Kim [8]. Although slip is considered along both the streamwise and spanwise directions, the shear-dependence of the slip length is only modelled along the streamwise direction because this direction experiences the highest shear. The turbulent flow is studied numerically by DNS, carried out by the Incompact3d code [39, 40].

The first objective is to solve the Navier-Stokes equations analytically for the laminar flows in the confined channel-flow and pipe-flow geometries. The laminar channel flow is then studied through nonlinear Lyapunov stability analysis. The rigorous two-dimensional approach by Balogh *et al.* [41] is extended to the three-dimensional case and the shear-dependent laminar solution is chosen as the base flow. We stress that, although not useful to explain the physics of drag reduction in the turbulent regime because of the very small critical Reynolds number, the stability analysis is useful to arrive at rigorous nonlinear stability conditions. The feedback-control wall boundary conditions found from the stability analysis coincide with the hydrophobic slip-length model. For the first time, the conceptual link between the extracted feedback-law boundary conditions and the hydrophobic-surface model is advanced.

Other objectives are to extend the theory of Fukagata *et al.* [6] to the shear-dependent slip-length case, to evince how the parameters describing the hydrophobic surface affect the drag reduction rate, and to carry out a comparison between Fukagata *et al.* [6]'s theoretical results and the DNS results. The final aim is to study the drag-reducing turbulent flow through statistical analysis. The power exerted by the liquid turbulent flow on the hydrophobic surface is investigated and the principal strain rates of the near-wall turbulent flow are studied for the first time in a drag-reducing flow.

In §II, the laminar-flow analysis is presented. The laminar flow solutions for the channel-flow and the pipe-flow geometries are found in §II A and the Lyapunov stability analysis is discussed in §II B. In §III, the turbulent-flow analysis is presented. The Fukagata *et al.* [6]'s theory for drag-reduction prediction is contained in §III B, the results on the drag reduction properties and turbulence statistics are found in §III C, and the power spent on the hydrophobic surface is discussed in §III D. In §III E, the numerical results on the turbulent vorticity are presented and the study of the principal strain rates is found in §III F. In §IV a summary of the results is given.

II. LAMINAR FLOW

This section presents the analytical results for laminar flows over hydrophobic surfaces in §II A and the nonlinear Lyapunov stability analysis of the laminar channel flow in §II B.

A. Analytical laminar solutions

The laminar channel-flow solution with shear-dependent slip-length hydrophobic walls is first derived analytically. Lengths are scaled by the channel half-height h^*, velocities by the maximum Poiseuille velocity U_p^* with uncontrolled walls, and the time t^* by h^*/U_p^*. Quantities non-dimensionalized through these units are not indicated by any symbol and dimensional quantities are marked by the superscript $*$. The Reynolds number is defined as $R_p = U_p^* h^*/\nu^*$, where ν^* is the kinematic viscosity of the fluid. The streamwise, wall-normal, and spanwise directions are x^*, y^*, and z^*, respectively, and $y \in [0, 2]$. The velocity vector field is defined as $\mathbf{W} = (U(x, y, z, t), V(x, y, z, t), W(x, y, z, t))$ and the pressure is $P(x, y, z, t)$. The velocity and the pressure satisfy the incompressible continuity and Navier-Stokes equations. The hydrophobic surface is modelled through the following boundary condition at the bottom wall:

$$U(0) = l_s \left.\frac{\partial U}{\partial y}\right|_{y=0} = a \left(\left.\frac{\partial U}{\partial y}\right|_{y=0} \right)^2 + b \left.\frac{\partial U}{\partial y}\right|_{y=0}, \tag{1}$$

and analogously for the upper wall at $y = 2$. The constant b is positive and, as suggested by experiments [8, 32, 33], a is also positive. The boundary condition (1) is also consistent with the shear-dependent slip length computed from the molecular dynamics simulations carried out by Thompson and Troian [42], i.e., $l_s = l_{s0}(1 - \dot{\gamma}/\dot{\gamma}_c)^{-1/2}$, where $\dot{\gamma}$ and $\dot{\gamma}_c$ are the scaled shear rate and a critical shear rate, respectively. Indeed, the Taylor expansion for small $\dot{\gamma}$ leads to $l_s = l_{s0} + l_{s0}\dot{\gamma}/(2\dot{\gamma}_c) + \mathcal{O}(\dot{\gamma}^2)$. As the flow is symmetric along the channel centreline, the other boundary condition may be chosen as:

$$\left.\frac{\partial U}{\partial y}\right|_{y=1} = 0. \tag{2}$$

In the case of fully-developed two-dimensional laminar channel flow, $\mathbf{W} = (U(y), 0, 0)$. The streamwise velocity U satisfies a simplified form of the x-momentum equation,

$$\frac{1}{R_p}\frac{\mathrm{d}^2 U}{\mathrm{d}y^2} - \frac{\mathrm{d}P}{\mathrm{d}x} = 0. \tag{3}$$

The solution is

$$U(y) = R_p \frac{\mathrm{d}P}{\mathrm{d}x}\left(\frac{y^2}{2} - y + aR_p\frac{\mathrm{d}P}{\mathrm{d}x} - b\right). \tag{4}$$

It is useful to introduce the bulk velocity,

$$\mathcal{U}_b = \frac{1}{2}\int_0^2 U(y)\mathrm{d}y = R_p\frac{\mathrm{d}P}{\mathrm{d}x}\left(aR_p\frac{\mathrm{d}P}{\mathrm{d}x} - b - \frac{1}{3}\right). \tag{5}$$

The special case of constant slip length (a=0) is first studied. In the constant-bulk-velocity case, $\mathcal{U}_b = 2/3$. The streamwise pressure gradient is

$$\frac{\mathrm{d}P}{\mathrm{d}x} = \frac{-2}{R_p(3b+1)}. \tag{6}$$

To enforce the same mass flow rate, the hydrophobic surface leads to a smaller pressure gradient than in the uncontrolled case. The pressure gradient tends to zero as b increases. By substituting (6) into (4), for $a = 0$ one finds

$$U(y) = \frac{-2}{3b+1}\left(\frac{y^2}{2} - y - b\right), \tag{7}$$

which was also derived by Min and Kim [5]. In the limit of large slip length, $b \to \infty$, the plug flow case is found, $U = \mathcal{U}_b$. For the case of constant pressure gradient, $\mathrm{d}P/\mathrm{d}x = -2/R_p$. For $a = 0$, $\mathcal{U}_b$ increases linearly with the slip length, $\mathcal{U}_b = 2b + 2/3$.

In the shear-dependent slip-length case, $a \neq 0$, and when $\mathcal{U}_b$ is constant, the pressure gradient is found as follows. Expression (5) is first solved for the pressure gradient,

$$\left.\frac{\mathrm{d}P}{\mathrm{d}x}\right|_{1,2} = \frac{3b+1}{6aR_p}\left[1 \pm \sqrt{1 + \frac{36a\mathcal{U}_b}{(3b+1)^2}}\right]. \tag{8}$$

The minus-sign solution is selected by Taylor expansion of the square-root term in (8) for small a and $b = \mathcal{O}(1)$, i.e., $[1 + 36a\mathcal{U}_b/(3b+1)^2]^{1/2} = 1 + 18a\mathcal{U}_b/(3b+1)^2 + \mathcal{O}(a^2)$, to match (8) with the pressure-gradient solution (6) for the constant-slip-length case. We further set $\mathcal{U}_b = 2/3$ and the result is

$$\frac{\mathrm{d}P}{\mathrm{d}x} = \frac{3b+1}{6aR_p}\left[1 - \sqrt{1 + \frac{24a}{(3b+1)^2}}\right]. \tag{9}$$

For $b = \mathcal{O}(1)$ and $a \to \infty$,

$$\frac{\mathrm{d}P}{\mathrm{d}x} \sim \frac{1}{R_p}\sqrt{\frac{2}{3a}}, \tag{10}$$

i.e., the pressure gradient is independent of b and decreases as a increases more slowly than when b increases and $a = 0$, as shown by (6). When the pressure gradient is constant, $\mathcal{U}_b = 4a + 2b + 2/3$, that is the bulk velocity increases linearly with both a and b, and the growth rate is larger for a. The equivalent slip length can be computed in the laminar case by substituting (4) into (1), i.e.,

$$l_s = b - aR_p\frac{\mathrm{d}P}{\mathrm{d}x}. \tag{11}$$

The solution for the laminar flow in a pipe with a hydrophobic wall featuring a shear-dependent slip length is studied in Appendix A. The bulk velocity is related to the pressure gradient as follows

$$\mathcal{U}_b = 2\int_0^1 U(r)r\mathrm{d}r = \frac{R_p}{8}\frac{\mathrm{d}P}{\mathrm{d}x}\left(2aR_p\frac{\mathrm{d}P}{\mathrm{d}x} - 4b - 1\right), \tag{12}$$

where the pipe-flow quantities in (12) are defined in Appendix A. The relationship (12) is useful to compute the slip-length parameters a and b from the experimental data of mass flow rate of mercury in thin quartz capillaries as a function of the pressure gradient reported by Churaev *et al.* [33] in their figure 4 on page 579 and reproduced in figure 1 (left). It is clear that a constant-slip-length behaviour only occurs at small pressure gradients (dashed line), while a quadratic behaviour as that predicted by (12) ensues for larger pressure gradients (solid line). By rescaling (12)

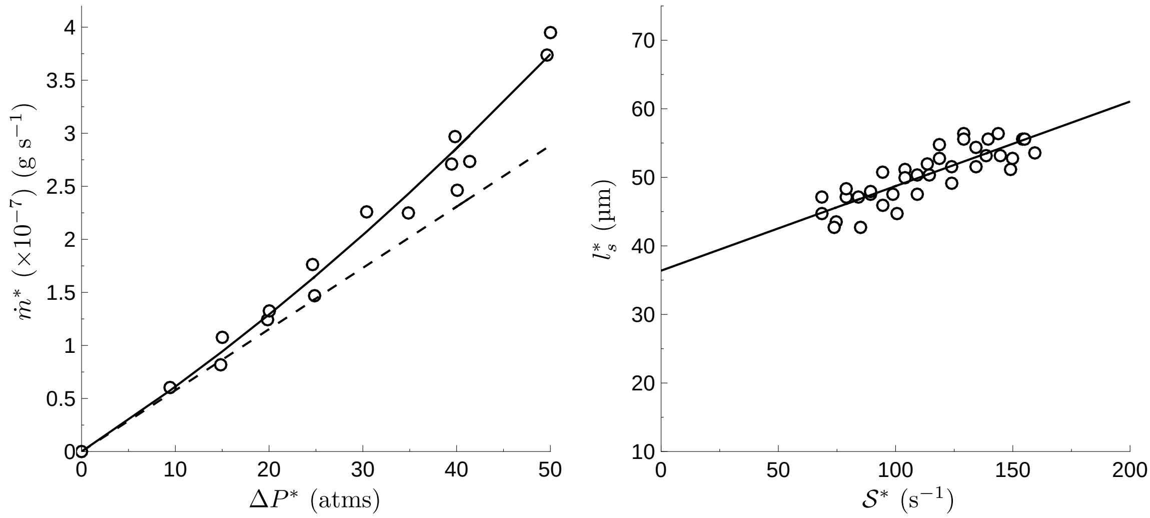

FIG. 1: Left: Mass flow rate as a function of pressure difference for mercury flow in thin quartz capillary tubes, measured by Churaev *et al.* [33] (refer to their figure 4 on page 579). Right: Slip length as a function of shear rate for water flow in a cone-and-plate rheometer, measured by Choi and Kim [8] (refer to their figure 4).

and fitting the experimental data, a^*=7·10^{-6}μm s and b^*=0.16μm are found. We are also interested in laminar flows over surfaces characterized by larger slip lengths[3], i.e., of the order of tens of μm. To the best of our knowledge, the cone-and-plate rheometer data for a NanoTurf superhydrophobic surface reported by Choi and Kim [8] are the only ones that show shear-dependent slip lengths of this magnitude in the laminar regime (refer to their figure 4 (bottom)). As shown in figure 1 (right), the dependence of the slip length on the shear rate is linear with a^*=0.12μm s and b^*=36μm. Note that, although featuring slip lengths of different orders of magnitude, both Churaev *et al.* [33] and Choi and Kim [8] show a linear dependence of the slip length on the wall-shear stress, i.e., consistent with our model (1).

B. Nonlinear Lyapunov stability analysis

The Lyapunov nonlinear stability analysis of the laminar flow studied in §II A is performed in this section. The objective is to stabilize the channel flow around the chosen equilibrium point, i.e., (4), the solution of the laminar channel flow with hydrophobic walls featuring a shear-dependent slip length. The work by Balogh *et al.* [41] on the stabilization of a two-dimensional channel flow is extended to the three-dimensional space. At the end of the analysis, this approach allows the specification of an a-priori-unknown feedback-control boundary conditions at the wall. We find that these feedback-control boundary conditions are the same as those of the slip-length hydrophobic model.

The flow domain is $\Omega = \{(x, y, z) \in [0, L_x) \times [0, 2] \times [0, L_z)\}$. Periodic boundary conditions are applied to the homogeneous x and z directions. The L^2 norm of a vector $\boldsymbol{f}$ is defined as

$$||\boldsymbol{f}\,||_{L^2} = \sqrt{[|\boldsymbol{f}\,|^2]_{\mathcal{I}xyz}}, \tag{13}$$

where

$$[\cdot]_{\mathcal{I}xyz} = \int_0^{L_z}\int_0^{2}\int_0^{L_x} \cdot \; \mathrm{d}x\,\mathrm{d}y\,\mathrm{d}z. \tag{14}$$

The perturbation velocity vector, $\mathbf{w} = (u, v, w)$, and the perturbation pressure p are defined as:

$$u = U - \widehat{U}\ ,\ v = V - \widehat{V}\ ,\ w = W - \widehat{W}\ ,\ p = P - \widehat{P}, \tag{15}$$

where

$$\left(\widehat{\mathbf{U}},\widehat{P}\right)=\left(\widehat{U},\widehat{V},\widehat{W},\widehat{P}\right)=\left(\widehat{U}(y),0,0,\widehat{P}(x)\right). \tag{16}$$

$\widehat{U}(y)$ is given by (4) and $\widehat{P}(x) = x\mathrm{d}P/\mathrm{d}x$, where $\mathrm{d}P/\mathrm{d}x$ is given in (9). We operate under constant mass flow rate conditions to have bounded $\widehat{U}(y)$. Upon substitution of (15) in the incompressible Navier-Stokes equations, the nonlinear perturbation equations are found,

$$\nabla\cdot\mathbf{w}=0, \tag{17}$$

$$\frac{\partial\mathbf{w}}{\partial t}+(\mathbf{w}\cdot\nabla)\left(\mathbf{w}+\widehat{\mathbf{U}}\right)+\left(\widehat{\mathbf{U}}\cdot\nabla\right)\mathbf{w}=-\nabla p+\frac{1}{R_p}\nabla^2\mathbf{w}. \tag{18}$$

The perturbation energy is defined through the L^2 norm of the perturbed velocity, i.e., $E(\mathbf{w}) = ||\mathbf{w}||^2_{L^2}$. The time derivative of $E(\mathbf{w})$ is

$$\frac{1}{2}\frac{\mathrm{d}E(\mathbf{w})}{\mathrm{d}t}=\left[u\frac{\partial u}{\partial t}\right]_{\mathcal{I}xyz}+\left[v\frac{\partial v}{\partial t}\right]_{\mathcal{I}xyz}+\left[w\frac{\partial w}{\partial t}\right]_{\mathcal{I}xyz}. \tag{19}$$

Each term in (19) is expanded separately using (17)-(18) and periodicity in the homogeneous directions. An upper bound is derived for the time derivative of the energy,

$$\frac{\mathrm{d}E(\mathbf{w})}{\mathrm{d}t}\leq-\frac{\alpha E(\mathbf{w})}{2}+\frac{2}{R_p}\left[u^2(x,0,z,t)+w^2(x,0,z,t)\right]_{\mathcal{I}xz}+\frac{2}{R_p}\left[\left[u\frac{\partial u}{\partial y}+w\frac{\partial w}{\partial y}\right]_0^2\right]_{\mathcal{I}xz}, \tag{20}$$

where

$$[\cdot]_{\mathcal{I}xz}=\int_0^{L_z}\int_0^{L_x}\cdot\,\mathrm{d}x\,\mathrm{d}z, \tag{21}$$

and $\alpha = {R_p}^{-1} - 4 + {R_p}^{-1}L_x^{-2} + {R_p}^{-1}L_z^{-2}$. The details of the derivation of (20) are found in Appendix B. The dimensions of the domain along the homogeneous directions, L_x and L_z, can be taken as infinitely large, which leads to $\alpha = {R_p}^{-1} - 4$. In the uncontrolled case ($u(x, 0, z, t) = w(x, 0, z, t) = 0$ and $u(x, 2, z, t) = w(x, 2, z, t) = 0$), $E(\mathbf{w})$ decays exponentially in time if $\alpha > 0$, i.e., $R_p < 1/4$. As in Balogh *et al.* [41], global stability is achieved not only by choosing the right range for R_p, but also by modifying the integral terms, which pertain to the boundaries. Following Balogh *et al.* [41]:

$$u(x,y_w,z,t)=(1-y_w)\,k\frac{\partial u}{\partial y}(x,y_w,z,t),\;\; w(x,y_w,z,t)=(1-y_w)\,k\frac{\partial w}{\partial y}(x,y_w,z,t), \tag{22}$$

where y_w=0 for the lower wall and y_w=2 for the upper wall. Substitution of (22) into (20) leads to

$$\begin{aligned}\frac{\mathrm{d}E(\mathbf{w})}{\mathrm{d}t}\leq&-\frac{\alpha E(\mathbf{w})}{2}-\frac{2}{R_p}\left(\frac{1}{k}-1\right)\left[u^2(x,0,z)+w^2(x,0,z)\right]_{\mathcal{I}xz}\\&-\frac{2}{kR_p}\left[u^2(x,2,z,t)+w^2(x,2,z,t)\right]_{\mathcal{I}xz}.\end{aligned} \tag{23}$$

By setting $k \in (0, 1]$, the perturbation energy E decays exponentially, thus achieving global asymptotic stabilization.

It is remarkable to note that the controller found in (22), i.e., based on distributed actuation that linearly relates the in-plane wall velocity to the wall-normal velocity gradient, coincides with the widely-used Navier's model of hydrophobic surfaces (Min and Kim [4], where both streamwise and spanwise slip velocities are considered). The constant k agrees with the slip length l_s, given in (1). To the best of our knowledge, this is the first time that this conceptual link between these two apparently unrelated areas has been advanced.

A further interesting observation can be put forward. In the stability analysis, boundary terms involving the perturbation pressure p, i.e., proportional to pu, pv, and pw, vanish either by periodicity along x and z or through the no-penetration condition imposed on the wall-normal velocity. If the latter condition is relaxed while the periodicity along x and z is maintained, a wall-based controller of the type $v = Ap$ can be designed, which has been used by Balogh *et al.* [43] to maximize mixing in a three-dimensional pipe flow. We note here that this wall-based linear relationship between the wall-normal velocity and pressure has also been employed successfully to model the interaction between the compressible flow of air and porous surfaces [44], where A plays the role of the admittance. High-precision experiments of these acoustic absorbing coatings [45, 46] have been shown to lead to the attenuation of the growth rate of the acoustic mode in high-Mach-number compressible laminar boundary layers. The velocity-pressure boundary condition has also been used to simulate an incompressible turbulent flow over porous surfaces [47]. This problem is obviously out of the scope of the present study, but, similar to the wall-parallel controller case, it is worthwhile to notice how a purely mathematical exercise, such as the stability analysis, helps us educe boundary conditions that synthesize controllers with precise counterparts in Nature.

The shear-dependent slip-length condition is now derived from (20). The boundary conditions are

$$u(x, y_w, z, t) = a\left(\frac{\partial u}{\partial y}\right)^2 (x, y_w, z, t) + (1 - y_w)\, b\frac{\partial u}{\partial y}(x, y_w, z, t) \tag{24}$$

and corresponding ones for the spanwise velocity component w. Note that the different signs only apply to b and not to a because a multiplies $(\partial u/\partial y)^2$ and therefore the symmetrical condition over the two channel walls is respected. Following the same reasoning as in the constant k case, expressions for $\partial u/\partial y$ and $\partial w/\partial y$ are found from (24) and from the corresponding ones for w. In the shear-dependent slip-length case, the inequality for the perturbation energy is:

$$\begin{aligned}\frac{\mathrm{d}E(\mathbf{w})}{\mathrm{d}t} \leq & -\frac{\alpha E(\mathbf{w})}{2} - \frac{2}{R_p}\left(\frac{2}{b+\sqrt{b^2+4a}} - 1\right)\left[u^2(x,0,z,t) + w^2(x,0,z,t)\right]_{\mathcal{I}xz} \\ & - \frac{4}{R_p\left(b+\sqrt{b^2+4a}\right)}\left[u^2(x,2,z,t) + w^2(x,2,z,t)\right]_{\mathcal{I}xz}.\end{aligned} \tag{25}$$

The derivation is detailed in Appendix C. In the limit $a \to 0$, (23) is recovered from (25). As the limits $L_x, L_z \to \infty$ have been taken, $\left[u^2(x,0,z,t) + w^2(x,0,z,t)\right]_{\mathcal{I}xz} = \left[u^2(x,2,z,t) + w^2(x,2,z,t)\right]_{\mathcal{I}xz}$. It follows that (25) simplifies to:

$$\frac{\mathrm{d}E(\mathbf{w})}{\mathrm{d}t} \leq -\frac{\alpha E(\mathbf{w})}{2} - \frac{2}{R_p}\left(\frac{4-b-\sqrt{b^2+4a}}{b+\sqrt{b^2+4a}}\right)\left[u^2(x,0,z,t) + w^2(x,0,z,t)\right]_{\mathcal{I}xz}. \tag{26}$$

In summary, the stability conditions are

$$R_p < \frac{1}{4}, \quad a \leq 4 - 2b, \quad a \leq b^2/4. \tag{27}$$

The first stability condition relating the positive a and b in (27) is found by imposing the coefficient multiplying the second term on the right-hand-side in (26) to be negative. The inequality changes to the more restrictive $a \leq 1 - b$ if (25) is used. The last stability condition in (27) is derived in Appendix C (refer to analysis leading to (C4)). As in the two-dimensional case studied by Balogh *et al.* [41], the condition on the Reynolds number is very restrictive and proper of laminar microfluidic flows. Therefore, the nonlinear stability analysis does not provide information on the physical mechanism that leads to the attenuation of the turbulent kinetic energy.

We can verify whether the flow parameters in Choi and Kim [8], pertaining to a laminar flow in a thin gap between a stationary plate and a spinning cone (i.e., a very good model for the idealized Couette flow), satisfy our stability conditions (27) because these are also valid for Couette flow (which is verified by substituting the Couette constant shear in inequality (B17)). A Reynolds number of 1/4, based on their rheometer's gap and tip speed, is found for an angular velocity of 0.15 rad/s, which is in the range of values that the rheometer can achieve. By scaling their slip parameters, a^*=0.12µm s and b^*=36µm, by the rheometer's tip speed and gap thickness, the first stability condition, $a \leq 4 - 2b$, is always satisfied. The second condition, $a \leq b^2/4$, is satisfied when the rheometer's tip speed is smaller than 0.029 m/s (angular velocity smaller than 0.6 rad/s), which again is in the realizable range of Choi and Kim [8]'s experimental rig.

III. TURBULENT FLOW

The turbulent flow decomposition and the numerical procedures are contained in §III A and the Fukagata-Kasagi-Koumoutsakos theory for drag reduction prodiction is described in §III B. The numerical results are found in the remaining §III C-§III F.

A. Turbulent flow decomposition and numerical procedures

The turbulent flow is decomposed into a mean and a fluctuating component,

$$(U, V, W) = (\mathcal{U}(y), 0, 0) + (u', v', w')\,, \tag{28}$$

where the mean streamwise flow is

$$\mathcal{U}(y) = (L_x L_z)^{-1} \left[\overline{U}\right]_{\mathcal{I}xz}\,, \tag{29}$$

$$\overline{\cdot} = \frac{1}{t_f - t_i} \int_{t_i}^{t_f} \cdot \,\mathrm{d}t, \tag{30}$$

and t_i and t_f are the initial and finish times defining the interval for the time averaging. The skin-friction coefficient is defined as usual,

$$C_f = \frac{2\nu^*}{\mathcal{U}_b^{*2}} \left.\frac{\mathrm{d}\mathcal{U}^*}{\mathrm{d}y^*}\right|_{y=0} = \frac{2}{R_p \mathcal{U}_b^2} \left.\frac{\mathrm{d}\mathcal{U}}{\mathrm{d}y}\right|_{y=0}, \tag{31}$$

where the turbulent bulk velocity $\mathcal{U}_b$ in (31) is obtained by replacing $\mathcal{U}$ for U in (5). Unless otherwise specified, the notation $y = 0$ hereinafter indicates a quantity averaged over the two walls. The turbulent drag reduction $\mathcal{R}$ is

$$\mathcal{R}(\%) = 100\left(1 - \frac{C_f}{C_{f,r}}\right), \tag{32}$$

where the subscript r hereinafter denotes a quantity in the reference case of channel flow with uncontrolled walls. The friction Reynolds number is

$$R_\tau = \frac{u_\tau^* h^*}{\nu^*} = u_\tau R_p, \tag{33}$$

where

$$u_\tau = \sqrt{\frac{1}{R_p} \left.\frac{\mathrm{d}\mathcal{U}}{\mathrm{d}y}\right|_{y=0}} \tag{34}$$

is the friction velocity. Scaling by viscous units of the uncontrolled wall, i.e., $u_{\tau,r}^*$ and ν^*, is denoted by the superscript $+0$ and scaling by viscous units of the hydrophobic wall is indicated by the superscript $+$.

The root-mean-square (rms) of a fluctuating velocity component q' is defined as:

$$q_{rms} = \sqrt{(L_x L_z)^{-1} \left[\overline{q'^2}\right]_{\mathcal{I}xz}}. \tag{35}$$

The Reynolds stresses are defined as

$$uv_{rey} = (L_x L_z)^{-1} \left[\overline{u'v'}\right]_{\mathcal{I}xz}. \tag{36}$$

The power balance within the channel can be written as:

$$\mathcal{P}_x + \mathcal{W} + \mathcal{D} = 0, \tag{37}$$

where $\mathcal{P}_x$ is the power spent to pump the fluid along x, $\mathcal{W}$ is the power spent by the viscous action of the fluid on the hydrophobic surface, and $\mathcal{D}$ is the viscous dissipation of kinetic energy into heat. For cases for which the wall no-penetration condition is imposed on the wall-normal velocity component and slip is considered only along the streamwise direction, the three quantities in (37) are:

$$\mathcal{P}_x = 2\mathcal{U}_b L_x L_z \left(\frac{R_\tau}{R_p}\right)^2, \tag{38}$$

$$\mathcal{W} = -\frac{2}{R_p}\left[\overline{U(0)\left.\frac{\partial U}{\partial y}\right|_{y=0}}\right]_{\mathcal{I}xz}, \tag{39}$$

and

$$\mathcal{D} = -\frac{1}{R_p}\left[\overline{\left(\frac{\partial U_i}{\partial x_j}+\frac{\partial U_j}{\partial x_i}\right)\frac{\partial U_i}{\partial x_j}}\right]_{\mathcal{I}xyz}, \tag{40}$$

where the Einstein summation convention of repeated indices is used. The percent power used by the fluid on the surface is $\mathcal{P}_{sp}(\%) = 100\mathcal{W}/\mathcal{P}_{x,r}$. Appendix D details the derivation of the energy terms (38), (39), and (40).

The pressure-driven turbulent flow between infinite parallel flat plates with hydrophobic properties has been studied by DNS at low Reynolds number. The open-source Navier-Stokes solver Incompact3d [39, 40], freely available on the Internet at `http://www.incompact3d.com/`, has been modified to model the hydrophobic surfaces characterized by constant and shear-dependent slip lengths. The present simulations have been performed on the Polaris cluster at the University of Leeds and the ARCHER UK National Supercomputing Service.

The simulations have been carried out at $R_p = 4200$ at constant mass flow rate, i.e., $\mathcal{U}_b = 2/3$, and the uncontrolled friction Reynolds number is $R_{\tau,r} = 179.5$. The dimensions of the computational domain are $L_x = 4\pi$, L_y=2, and $L_z = 4\pi/3$. The time step is $\Delta t = 0.0025$ ($\Delta t^{+0} = 0.019$). The grid sizes are $\Delta x^{+0} = 8.5$ and $\Delta z^{+0} = 3$, and the minimum $\Delta y^{+0} = 0.4$ near the wall. The simulations with hydrophobic walls have been started from a fully-developed turbulent flow with the no-slip condition. As in Ricco and Hahn [48], the turbulence statistics are computed after discarding the initial temporal transient during which the flow adapts to the new drag-reducing regime. The duration of the transient is estimated by direct observation of the time history of the space-averaged wall-shear stress and is typically of the order of $100h^*/U_p^*$ ($1150\nu^*/u_{\tau,r}^{*2}$). The statistics are calculated by averaging instantaneous flow fields saved at intervals of $10\nu^*/u_{\tau,r}^{*2}$ for a total time window of $850h^*/U_p^*$ ($6520\nu^*/u_{\tau,r}^{*2}$).

In the code, 6^{th}-order compact finite difference schemes are used for the spatial derivatives in the convective and diffusive terms. For the modelling of the hydrophobic surfaces, the wall boundary conditions (24) are implemented through single-sided two- and three-point formulas. Both schemes have been tested thoroughly without notable differences. The constant-slip-length results have been compared successfully with Min and Kim [4]'s and Busse and Sandham [9]'s.

B. Fukagata-Kasagi-Koumoutsakos theory for a turbulent flow over shear-dependent slip-length surfaces

The theoretical analysis by Fukagata *et al.* [6] (FKK hereinafter) is extended to the case of shear-dependent slip length. As in the constant-slip-length case used in FKK, the starting point is to express the mean streamwise slip velocity $\mathcal{U}(0)$ as a function of the wall-normal gradient of the mean velocity:

$$\mathcal{U}(0) = a\left(\left.\frac{\mathrm{d}\mathcal{U}}{\mathrm{d}y}\right|_{y=0}\right)^2 + b\left.\frac{\mathrm{d}\mathcal{U}}{\mathrm{d}y}\right|_{y=0}. \tag{41}$$

Note that in the constant-slip-length case ($a = 0$), (41) is found from (1) because the order of the integral operators used in (29) and the wall-normal derivative operator can be switched as the relationship is linear. In the shear-dependent case, this is obviously not possible because of the square of the wall-normal gradient. To make progress and continue along the lines of FKK's theoretical formulation, (41) is nevertheless assumed to hold. Appendix E proves that the error in assuming (41) to be valid is less than 1%.

Equation (41) is first transformed into:

$$\mathcal{U}(0)^+ = a u_{\tau,r}\left(R_{\tau,r}\left.\frac{\mathrm{d}\mathcal{U}^+}{\mathrm{d}y^+}\right|_{y=0}\right)^2\left(u_\tau^{+0}\right)^3 + b\left.\frac{\mathrm{d}\mathcal{U}^+}{\mathrm{d}y^+}\right|_{y=0} u_\tau^{+0} R_{\tau,r}. \tag{42}$$

As $\mathrm{d}\mathcal{U}^+/\mathrm{d}y^+|_{y=0} = 1$, then using $u_\tau = u_\tau^{+0} u_{\tau,r}$ and $\mathcal{U}(0) = \mathcal{U}(0)^+ u_\tau^{+0} u_{\tau,r}$, (42) becomes

$$\mathcal{U}(0) = a\left(u_\tau^{+0}\right)^4\left(u_{\tau,r}R_{\tau,r}\right)^2 + b\left(u_\tau^{+0}\right)^2 u_{\tau,r}R_{\tau,r}. \tag{43}$$

The bulk velocity, $\mathcal{U}_b$, is expressed as the sum of the mean slip velocity and an effective bulk velocity $\mathcal{U}_{be}$,

$$\mathcal{U}_b = \mathcal{U}(0) + \mathcal{U}_{be}. \tag{44}$$

The bulk velocity is assumed to satisfy Dean [49]'s formula,

$$\mathcal{U}_b = \left(\kappa^{-1} \ln R_{\tau,r} + F\right) u_{\tau,r}, \tag{45}$$

where both the constant F and the von Kármán constant κ are assumed to be independent of the Reynolds number. Formula (45) follows directly from the assumption that the mean-velocity profile is logarithmic in the channel core. As amply verified by experimental and numerical data [50–52], this is not the case at the low Reynolds number of the present study and it has been argued that a truly logarithmic behaviour is only obtained at an infinite Reynolds number [52]. Nevertheless, the use of (45) has proved to be successful in the constant-slip-length cases as excellent theoretical predictions for $\mathcal{R}$ were obtained by FKK. Therefore, the logarithmic behaviour is also assumed to hold in the present shear-dependent slip-length cases and the predictive power of the framework is checked a posteriori when the theoretical results are compared with the DNS data in §III C.

As suggested by Busse and Sandham [9], κ and F are computed from our DNS data. The von Kármán constant κ is estimated through the diagnostic function [50, 52]:

$$\kappa^{-1} = y^+ \frac{\mathrm{d}\mathcal{U}^+}{\mathrm{d}y^+}. \tag{46}$$

Once κ is known, F is computed via (45). We find $\kappa = 0.4$ and $F = 2.67$. As in FKK, the effective bulk velocity is also assumed to follow the logarithmic law,

$$\mathcal{U}_{be} = \left[\kappa^{-1} \ln\left(u_\tau^{+0} R_{\tau,r}\right) + F\right] u_\tau^{+0} u_{\tau,r}. \tag{47}$$

Combining equations (43) and (47), one finds

$$\left(\kappa^{-1} \ln R_{\tau,r} + F\right) \frac{1 - u_\tau^{+0}}{\left(u_\tau^{+0}\right)^2} = a \left(u_\tau^{+0}\right)^2 u_{\tau,r} {R_{\tau,r}}^2 + b R_{\tau,r} + \frac{\ln u_\tau^{+0}}{\kappa u_\tau^{+0}}. \tag{48}$$

Using $u_\tau^{+0} = \sqrt{1 - \mathcal{R}^\star}$, $\mathcal{R}^\star = \mathcal{R}/100$ and $u_{\tau,r} = R_{\tau,r}/R_p$, (48) becomes

$$\frac{a\left(1 - \mathcal{R}^\star\right) R_{\tau,r}^2}{R_p} + b = \left(\kappa^{-1} \ln R_{\tau,r} + F\right) \frac{1 - \sqrt{1 - \mathcal{R}^\star}}{R_{\tau,r}(1 - \mathcal{R}^\star)} - \frac{\ln\left(1 - \mathcal{R}^\star\right)}{2\kappa R_{\tau,r}\sqrt{1 - \mathcal{R}^\star}}. \tag{49}$$

The value of $\mathcal{R}^\star$ is found through a Monte Carlo simulation [53]. As expected, the constant-slip-length formula (13) in FKK is recovered from (49) when $a = 0$. There is an interesting interpretation of the left-hand-side of (49). It can be written as follows:

$$\frac{a\left(1 - \mathcal{R}^\star\right) R_{\tau,r}^2}{R_p} + b = a \left.\frac{\mathrm{d}\mathcal{U}}{\mathrm{d}y}\right|_{y=0} + b = b - a\frac{\mathrm{d}P}{\mathrm{d}x} R_p = \mathcal{L}_1. \tag{50}$$

It represents the averaged slip length $\mathcal{L}_1$, as defined in (E4). Therefore the extended FKK equation (49) has the same form of the original FKK equation where $\mathcal{L}_1$ replaces the constant slip length b. Also, once written in terms of the pressure gradient $\mathrm{d}P/\mathrm{d}x$, the average slip length has the same form of the equivalent slip length of the laminar case given in (11). It follows that turbulent flows with the same averaged slip length are characterized by the same reduction of wall friction. In §III C, this property is successfully checked via DNS and the $\mathcal{R}$ values computed from (49) for different a and b values are compared with the DNS data.

C. Turbulent drag reduction and velocity statistics

Numerical simulations in the shear-dependent slip-length cases are carried out by first varying a and b, the constants for the hydrophobic model along the streamwise direction. Figure 2 shows the very good comparison between the $\mathcal{R}$ values computed via DNS (black circles) and the theoretical predictions obtained through the FKK theory (solid lines), studied in §III B.

The drag reduction increases monotonically with a for fixed b and with b for fixed a. For fixed a, the growth of $\mathcal{R}$ as b increases is more intense for small a values and the drag reduction has a very weak dependence on a for $a \leq 10^{-4}$. For $b = 0.02$ and a increasing from $a = 0.001$ to $a = 0.01$, the drag reduction increases from $\mathcal{R} = 33.4\%$ to $\mathcal{R} = 51\%$, which is the maximum $\mathcal{R}$ computed in our study.

As discussed in §III B, an averaged slip length $\mathcal{L}$ is defined (refer to Appendix E). For $b = 0.02$ and a increasing from $a = 0.001$ to $a = 0.01$, the average slip length $\mathcal{L}$ increases from 0.025 ($\mathcal{L}^{+0} = 4.52$) to 0.06 ($\mathcal{L}^{+0} = 10.5$). Flows with the same $\mathcal{L}$ have the same drag reduction, which is verified even when two extreme cases at the maximum $\mathcal{R}$=51% with the same $\mathcal{L} = 0.06$, one with $a = 0.0159$ and $b = 0$ and the other with $a = 0$ and $b = 0.06$, are compared. For this to occur, we notice that $\mathcal{L}^*$ is scaled in outer units and not in viscous units of the hydrophobic case. Our results with $a \neq 0$ agree with the constant-slip-length ones by Min and Kim [4] and Busse and Sandham [9] for the same $\mathcal{L}$.

These numerical results confirm the theoretical prediction of monotonic growth of $\mathcal{R}$ with $\mathcal{L}$, given by the FKK equation (49) once (50) is used. From the definition of $\mathcal{L}$ given in Appendix E and from the agreement of $\mathcal{R}$ values for the same $\mathcal{L}$, it also follows that flows with the same $\mathcal{L}$ have the same averaged wall-slip velocity $\mathcal{U}(0)$. From the Fukagata-Iwamoto-Kasagi (FIK) identity [54], herein extended to include the effect of wall hydrophobicity [23, 28],

$$C_f = \frac{6}{\mathcal{U}_b R_p} - \frac{6}{\mathcal{U}_b^2}\int_0^1 (1-y) uv_{rey} \mathrm{d}y - \frac{6\,\mathcal{U}(0)}{R_p \mathcal{U}_b^2}, \tag{51}$$

it is found that flows with the same $\mathcal{R}$ and $\mathcal{U}(0)$ must have an equally weighted y-integrated contribution of the Reynolds stresses uv_{rey}. Our numerical calculations confirm this and further show that that the uv_{rey} profiles agree throughout the channel. However, despite the same uv_{rey}, the rms profiles of the velocity components do not overlap. For the cases with maximum $\mathcal{R}$=51% ($a = 0.0159$, $b = 0$ and $a = 0$, $b = 0.06$), the u_{rms} profiles differ up to $y = h/3$, their peaks show a 14% difference, and $u_{rms}(0)$ differ by 30%. This demonstrates that locally the behaviour of wall turbulence over these surfaces is markedly different and that the property of same $\mathcal{R}$ for same $\mathcal{L}$ is only to be considered in spatial and temporal averaged terms.

In the constant-slip case (a=0), the space- and time-averaged wall velocity $\mathcal{U}(0)$ has also been verified to agree with the following

$$\mathcal{U}(0) = \frac{3b}{3b+1}\left[\mathcal{U}_b - R_p \int_0^1 (1-y) uv_{rey} \mathrm{d}y\right], \tag{52}$$

which is found by averaging the wall boundary conditions (1) with $a = 0$, and by substitution of (31) into (51). As expected, $\lim_{b\to\infty} U(0) = \mathcal{U}_b$, i.e., the laminar plug-flow found in §II A is recovered because the Reynolds stresses vanish slowly when the turbulent production decreases as the mean-flow wall-normal gradient drops, as shown by Busse and Sandham [9].

The effect of slip along the spanwise direction is also considered. Along z, a constant slip length is considered ($a = 0$) because the wall-shear stress is smaller than along the streamwise direction. In all the tested cases, degradation of drag reduction is found, which confirms the original result by Min and Kim [4] for constant slip length along both directions. This effect is more intense for small $\mathcal{L}$. $\mathcal{R}$ decreases from 29% to 21.5% when, along x, $a = 0.0036$ and $b = 0$, and the b value along z changes from null to 0.02. $\mathcal{R}$ changes only from 51% to 48% when, along x, $a = 0.01$ and $b = 0.02$, and b along z again increases from null to 0.02.

The rms of the three velocity components and the Reynolds stresses are shown in figure 3 for increasing values of a and $b = 0.02$. The value of u_{rms} at the wall increases with a and the effect of the hydrophobic surface is to attenuate the turbulence activity through the domain, confirming the main results by Min and Kim [4] for the constant-slip-length case. The modification is strengthened as a increases, which is consistent with $\mathcal{R}$ becoming larger as the average slip length increases. The streamwise velocity is the less affected, while the wall-normal and the spanwise velocities are attenuated by the same amount. The Reynolds stresses uv_{rey} are the most affected, with the peak decreasing by more than 50%. Figure 4 shows the u_{rms} and uv_{rey} scaled with the viscous units of the hydrophobic flow. Near the wall, where the streamwise-velocity boundary conditions are altered, the u_{rms} display a marked differences, i.e., $u^+_{rms}(0)$ and the peak of u^+_{rms} grow with $\mathcal{L}$ as expected. The changes at higher wall-normal locations are less significant and are thus mostly due to the modification of the Reynolds number. The collapse of the Reynolds stresses is confined very near the wall.

It is paramount to verify that the cases studied above can be realized experimentally. The maximum $\mathcal{R}$ case is considered, for which $\mathcal{L}^{+0} = 10.5$. It is assumed that this scaled value corresponds to $\mathcal{L}^* = 100$µm, which is a sensible choice according to several experimental and theoretical works [7, 8, 20]. From these values of $\mathcal{L}^{+0}$ and $\mathcal{L}^*$ the ratio u^*_τ/ν^* can first be found. Assuming the liquid to be water (ν^*=10^{-6} m^{2}s^{-1}), the channel height $2h^* = 3.4$mm and the bulk velocity $\mathcal{U}^*_b$=1.6ms^{-1} can be educed from the Reynolds numbers $R_{\tau,r} = 180$ and $R_p = 4200$. These values

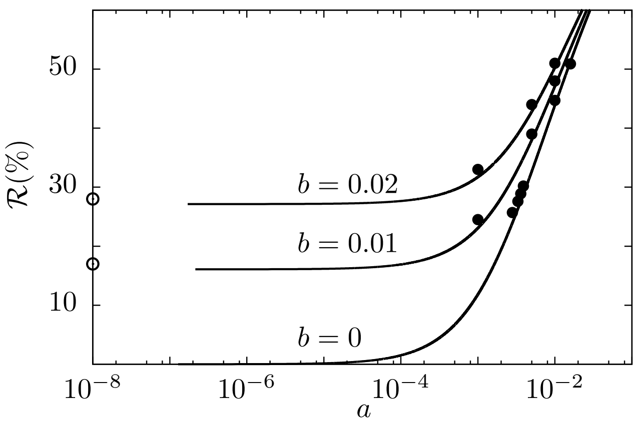

FIG. 2: Comparison between the $\mathcal{R}$ values computed via DNS (white circles for $a \to 0$ and black circles for finite a) and the theoretical prediction obtained through the modified FKK formula (49) (lines).

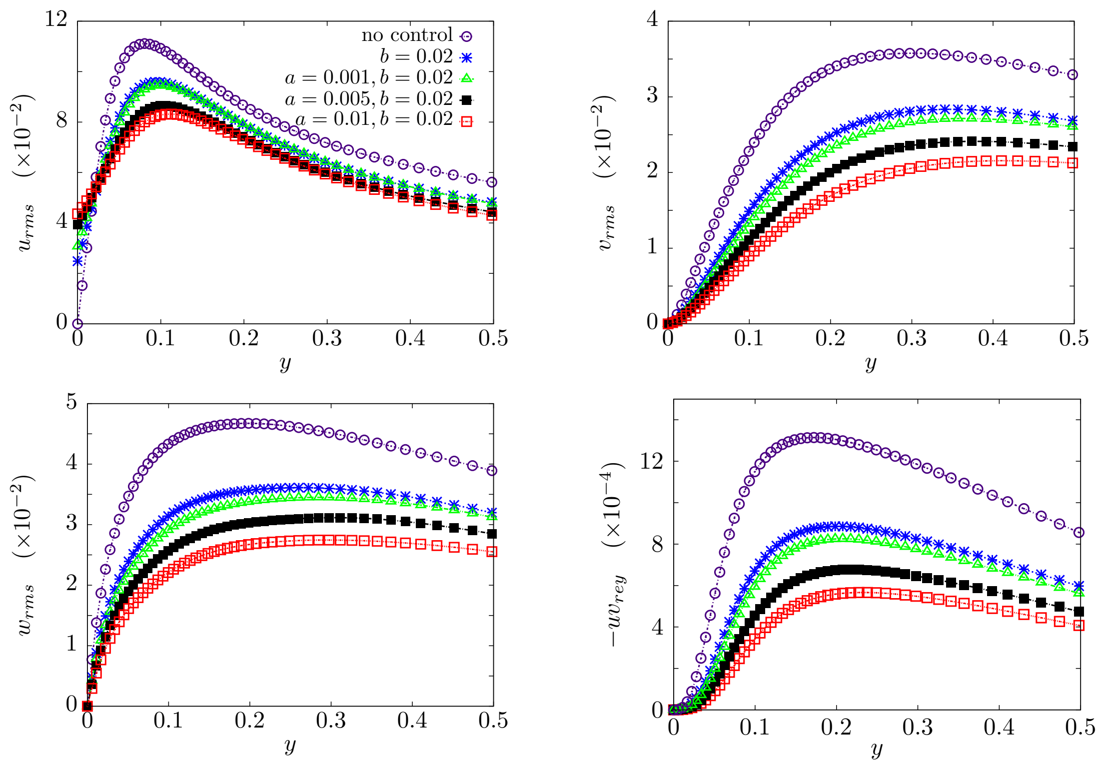

FIG. 3: Profiles of the rms of the streamwise (top left), wall-normal (top right) and spanwise (bottom left) velocity components and of the Reynolds stresses (bottom right), scaled in outer of the uncontrolled flow.

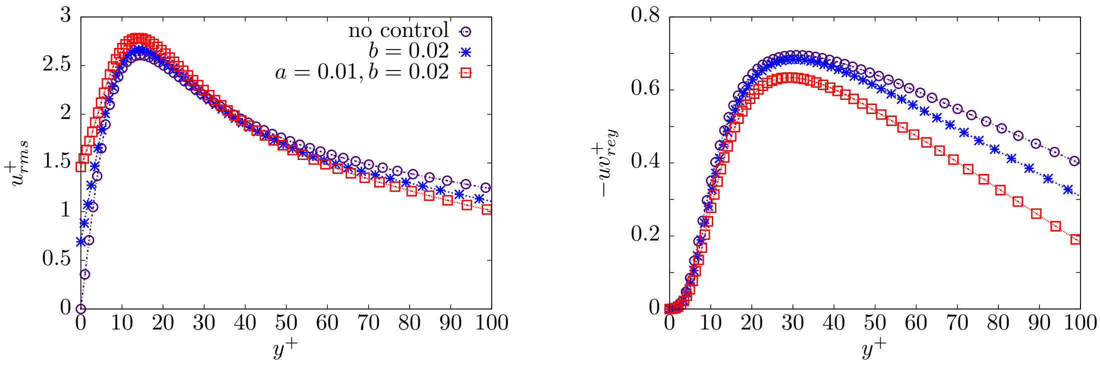

FIG. 4: Profiles of the rms of the streamwise velocity component (left) and of the Reynolds stresses (right), scaled with the viscous units of the hydrophobic flow.

fluid	ν^* ($\mathrm{m^2s^{-1}}$)	$R_{\tau,r}$	R_p	$2h^*$ (mm)	$\mathcal{U}_b$ ($\mathrm{ms^{-1}}$)
water	10^{-6}	180	4200	3.4	1.6
30% water+ glycerin	2.5×10^{-6}	180	4200	3.4	4.1
water	10^{-6}	400	10400	7.6	1.8
30% water+ glycerin	2.5×10^{-6}	400	10400	7.6	4.6
water	10^{-6}	1100	33060	20	2.1
30% water+ glycerin	2.5×10^{-6}	1100	33060	20	5.3

TABLE I: Estimates for the channel heights and the bulk velocities for different fluids and Reynolds numbers for $\mathcal{L}^* = 100\mu\mathrm{m}$ and $\mathcal{L}^{+0} = 10.5$.

can be realized in a laboratory. Table I shows more estimated values for channel-flow experiments, where the same slip lengths in viscous units and in physical dimensions are assumed (the empirical relationship $R_p = 11.05 R_{\tau,r}^{1.143}$ was used for the estimates at higher Reynolds numbers[55]). Our estimated flow quantities are comparable with those of Rosenberg *et al.* [15], who, for the first time, measured turbulent drag reduction (maximum $\mathcal{R} = 14\%$) in a Couette flow over SLIPS. The friction Reynolds number was $R_\tau = 140$, the maximum velocity was 4.4 m/s, and the gap thickness was 2 mm. Although no information was reported on whether their slip length depended on the shear rate, $\mathcal{L}^*$=138±55 µm ($\mathcal{L}^+ \approx 10$) is comparable to ours and to Choi and Kim [8]'s.

A further comment is due on the results by Choi and Kim [8], shown in figure 1 (right). By extrapolating the data, such surface would produce a slip length of 100µm when $\mathcal{S}^*$=450s^{-1}. We compare these quantities with our predictions in table I. For the first case in table I, b^*=36µm is assumed, $\mathcal{S}^*$ is about 10,000s^{-1} and a^*=0.01µm s. The shear rate is about 20 times larger Choi and Kim [8]'s and the constant of proportionality a^* is one order of magnitude smaller than Choi and Kim [8]'s. It follows that in a turbulent flow a much lower a than that found by Choi and Kim [8] would lead to significant shear-dependent effects because the wall-shear stress is much larger. This analysis proves that in wall-bounded turbulent flows, where the shear rate are orders of magnitude larger than in the laminar flows, hydrophobic surfaces are likely to feature slip lengths with shear dependence.

Further evidence of shear-dependent slip lengths emerges from the recent DNS investigation by Jung *et al.* [37], where turbulent channel flows at $R_{\tau,r} = 180$ over thin air layers have been simulated for the first time. Their figure 5f demonstrates that the slip length depends on the wall-shear stress for high-drag-reduction cases with zero mass flow rate in the air layer (refer to their figure 1b for a schematic of the flow domain). We have interpolated the data in their figure 5f with a power law, i.e., $u_s^{+0} = a_j (0.01\, \mu_r \partial u^{+0}/\partial y\big|_{y=0})^\beta$, where μ_r is the ratio between the viscosities of water and air. The least squares fitting method leads to $a_j = 0.006$ and $\beta = 2.02$. This means that for this type of idealized hydrophobic surfaces our boundary condition (24) with $b = 0$ and $a = 0.04$ (computed by rescaling a_j) is a very good model relating the instantaneous streamwise slip velocity and the streamwise velocity gradient at the water-air interface. According to our figure 2, this value of a would lead to $\mathcal{R}$ above 60%, which is consistent with the wall-shear stress reduction computed by Jung *et al.* [37]. It is certainly necessary to carry out further experimental and modeling work for flows at high wall-shear stress, especially in the turbulent flow regime, in line with the numerical study of Jung *et al.* [37] and the experimental study of Rosenberg *et al.* [15]. The main objectives would be to identify hydrophobic surfaces featuring shear-dependent slip lengths and to obtain further constitutive relations between the slip length and the shear rate.

D. Power spent by the turbulent flow on the hydrophobic surface

In wall-bounded flow control problems, the performance of a flow system must be evaluated by the drag reduction and by the power exchanged through the surface. To the best of our knowledge, this is the first time that $\mathcal{P}_{sp} = 100\mathcal{W}/\mathcal{P}_{x,r}$, i.e., the percent power that the fluid exerts on the hydrophobic surface with respect to the power required to pump the fluid along x in the uncontrolled case, is taken into account (refer to (38)-(39) and Appendix D for full derivation). This power is obviously null in the uncontrolled case. For the shear-dependent slip case with $a = 0.01$ and $b = 0.02$, $\mathcal{R} = 50\%$ and $\mathcal{P}_{sp} = 16\%$, and for the constant-slip case with $b = 0.02$ ($a = 0.0$), $\mathcal{R} = 29\%$ and $\mathcal{P}_{sp} = 12\%$.

In the case of a hydrophobic surface modelled by an alternating pattern of in-plane no-slip/free-shear strips without penetration, the power spent on the surface, given by equation (D5), is null because $U(0) = 0$ over solid portions of the wall and $\partial U/\partial y(0) = 0$ over air pockets [26]. In reality, the turbulent flow expends energy to shear the enclosed air pockets by viscous action. This power transfer is responsible for the detachment and disappearance of the air bubbles trapped in the surface, which leads to the degradation of its drag-reduction properties. As argued by Aljallis *et al.* [21] and Govardhan *et al.* [56], the loss of drag reduction is not due to surface damage, but to the high wall shear and pressure that cause the depletion of air from the wall, to a higher water-wetted area, and thereby drag increase. Further work is certainly needed to compare the power spent at the wall computed via the effective slip model and the power exerted by the flow on the air pockets. In the case of SLIPS [11, 15], power is instead expended by the flowing liquid onto the liquid substrate that infuses the rigid porous matrix, mainly by the shear stress at the interface between the two liquids.

An exchange of power at the surface in controlled wall-bounded turbulent flows obviously also occurs in several flow control techniques such as spanwise wall oscillation [57], wall travelling waves [58, 59], and spinning discs [48]. These are active methods because power is introduced into the fluid system from the exterior of the domain. This follows mathematically from the tangential velocity induced by the wall actuation decaying on average along y in a thin viscous layer within the turbulent flow. In the hydrophobic-surface case, a passive technique, power is instead exerted by the fluid on to the surface because, on average, both the slip-wall velocity and the wall-normal gradient of the streamwise velocity at the wall are positive. Therefore, $\mathcal{P}_{sp}$ for hydrophobic surfaces is of opposite sign when compared with that of active techniques. To compute the net power saved for active techniques, the power supplied at the wall $\mathcal{P}_{sp}$ is subtracted from the saved $\mathcal{P}_x$ (which coincides with $\mathcal{R}$ when the mass flow rate is constant), as discussed in Ricco and Hahn [48]. For the hydrophobic-surface case, the net power saved instead coincides with the saved $\mathcal{P}_x$ as $\mathcal{P}_{sp}$ is not supplied externally.

Passive techniques have often been classified as methods that do not involve exchange of energy through the boundaries. Riblets are one of these methods. Hydrophobic surfaces (and also compliant surfaces) can still be categorized as passive, although they absorb energy from the fluid in motion. Hydrophobic surfaces can thus be named passive-absorbing methods while geometry-modifying techniques, such as riblets, can be called passive-neutral.

Another point on the power spent ought to be discussed. As remarked in §II B after (23), the feedback boundary conditions extracted from the Lyapunov stability analysis coincide with those used to represent hydrophobic surfaces. Therefore two different physical systems are modelled through the same boundary conditions (22) and (24). In Balogh *et al.* [41], the boundary conditions are proposed to model an active technique for which the wall-shear stress is measured locally by distributed flush-mounted sensors to activate actuators which, in response to the wall-shear stress measurements, induce a wall streamwise velocity. As the boundary conditions in Balogh *et al.* [41]'s case and in the hydrophobic case coincide, Balogh *et al.* [41]'s surface absorbs power from the flow just like in the hydrophobic case. This sounds in contrast with Balogh *et al.* [41]'s idea of modelling an active drag reduction technique, which by definition requires an injection of power from the exterior of the system. This apparent contradiction is resolved if one accounts for the electrical and mechanical power spent by the sensors and actuators below the walls, which is not modelled by the boundary conditions (22) and (24).

E. Vorticity, vortices, and streaks

The rms of the vorticity vector components are shown in figure 5 for the uncontrolled, constant-slip-length, and shear-dependent slip-length cases. The graphs on the left show the profiles scaled in outer units, while the graphs on the right are nondimensionalized using viscous units based on the drag reduction friction velocity.

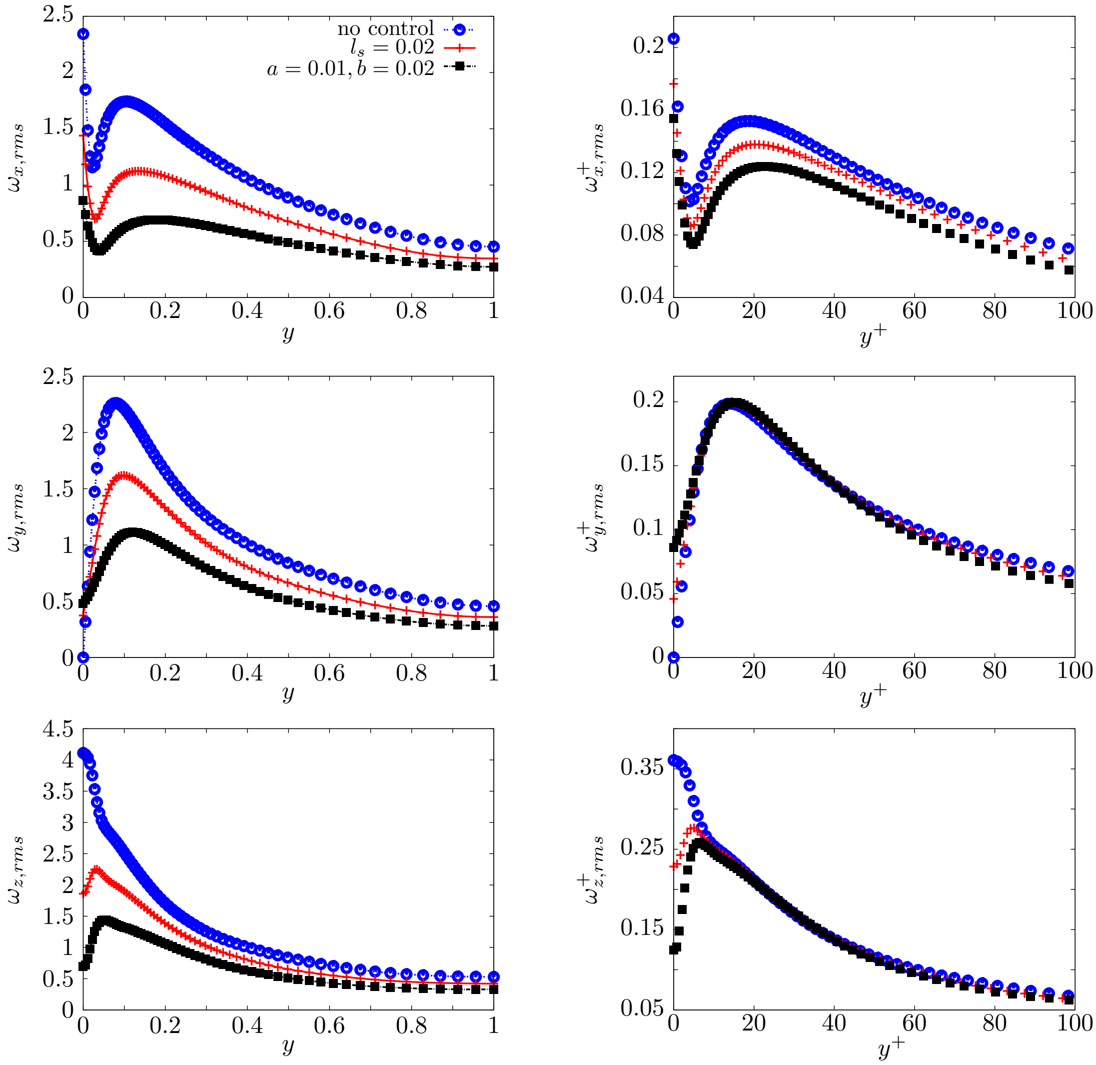

FIG. 5: Rms profiles of the streamwise (top), wall-normal (middle), and spanwise vorticity (bottom). Quantities in the left graphs are scaled by the uncontrolled $u_{\tau,r}$ and quantities in the right graphs are scaled by the drag-reducing u_τ.

In outer units, the fluctuations of all the vorticity components are strongly attenuated when compared to the uncontrolled case, indicating a strong reduction of turbulent activity. Like the uncontrolled case, the hydrophobic $\omega_{x,rms}$ profiles display a local minimum at the edge of the viscous sublayer and a higher local maximum, located in the buffer region, a sign of the presence of streamwise vortices [60]. The wall-normal position of the local minimum is only slightly moved upward, while the second maximum is more significantly shifted away from the wall in the hydrophobic case, a behaviour also observed in the opposition control flows [61, 62] and in flows over porous walls [47]. The attenuation and upward shift of $\omega_{x,rms}$ is consistent with the wall-shear stress reduction as high skin-friction regions are closely related to streamwise vortices [63]. When scaling in drag-reducing viscous units, a marked difference in the $\omega^+_{x,rms}$ profiles still occurs, particularly in the buffer region and beyond. This proves that these changes are not an effect of the friction Reynolds number, which decreases when the wall-shear stress is reduced, but the indication of a true flow modification throughout the whole channel.

The $\omega_{y,rms}$ and $\omega_{z,rms}$ profiles show a significant reduction throughout the channel for the hydrophobic cases when scaled in outer units. When scaled in viscous units, these profiles are only altered up to about $y^+ = 10$, showing very good collapse at higher locations. This demonstrates that, differently from the streamwise velocity, the changes

(a) (b)

FIG. 6: Low- (black) and high-speed (grey) streaks for the (a) no-slip and (b) shear-dependent slip-length cases at $y^{+0} = 12$ ($y = 0.07$), defined according to (53).

at $y^+ > 10$ are solely due to the change of Reynolds number caused by the drag reduction. The collapse of $\omega^+_{y,rms}$, which quantifies the alternation of low- and high-speed streamwise elongated regions, clearly shows that the low-speed streaks maintain their kinematic properties when scaled in viscous units. The strongest near-wall reduction is displayed by $\omega_{z,rms}$ as a direct consequence of the non-zero wall slip because ω'_z is dominated by $\partial u'/\partial y$ at the wall. These smaller fluctuations of $\omega_{z,rms}$ lead to a decrease of mean wall-shear stress via nonlinear interactions. A further comment on the velocity and vorticity statistics very near the wall ($y^+ < 10$) is due. Although the slip-length model is representative of either lotus-leaf-type surfaces with trapped air pockets or pitcher-plant-type SLIPS, very near the wall these statistics are likely not be the exact representation of the first kind of surfaces because of the spatial inhomogeneity of the texture (alternating solid patches and air pockets). However, they more precisely model the behaviour over SLIPS because the liquid infused in the porous substrate is homogeneously distributed as a thin layer below the overflowing liquid.

The low-speed streaks, streamwise-elongated regions of slow fluid compared to the mean flow [64, 65], are further analyzed to evince how these structures are affected by the hydrophobicity. Low- and high-speed streaks were defined as follows:

$$\text{Streak detection} \rightarrow \begin{cases} \text{Low speed if}: & u'(x,y,z,t) \leq -\chi \max\limits_{y} u_{rms}(y) \\ \text{High speed if}: & u'(x,y,z,t) \geq \chi \max\limits_{y} u_{rms}(y), \end{cases} \tag{53}$$

where $\chi = 0.9$ is the threshold parameter. Figure 6 shows the streaks in the $x - z$ plane at $y^{+0} = 12$ ($y = 0.07$), defined according to (53). The low-speed streaks over the hydrophobic surface appear more sporadically and more stretched along the streamwise direction than in the uncontrolled case. The high-speed streaks are also less numerous, more elongated, and wider than in the uncontrolled case.

To quantify the spreading of the low-speed streaks, we study the streamwise-velocity correlation functions along the spanwise direction $R_{uu,z}$, defined as

$$R_{uu,z}(\Delta z, y) = \frac{(L_x L_z)^{-1} \left[\overline{u'(x,y,z,t)u'(x,y,z+\Delta z,t)}\right]_{\mathcal{I}xz}}{u^2_{rms}}. \tag{54}$$

The correlation $R_{uu,z}$ is shown in figure 7 (left) for $y^{+0} = 12$ ($y = 0.07$). For the no-slip case, the first minimum is at $\Delta z^{+0} = 50$, resulting in the widely-reported streak spacing of 100 wall units [64, 65]. The minimum shifts to higher separation Δz, which indicates a larger spanwise streak spacing. The correlation $R_{uu,z}$ is also expressed versus Δz^+, scaled in drag-reducing viscous units, and shown in the inset of figure 7 (left). The uncontrolled, constant and shear-dependent models collapse on top of each other and present a minimum at $\Delta z^+ = 50$. This confirms the results of drag-reduction viscous scaling shown in figure 5 by $\omega^+_{y,rms}$, which is a measure of the alternating high and low streamwise velocity fluctuations near the wall.

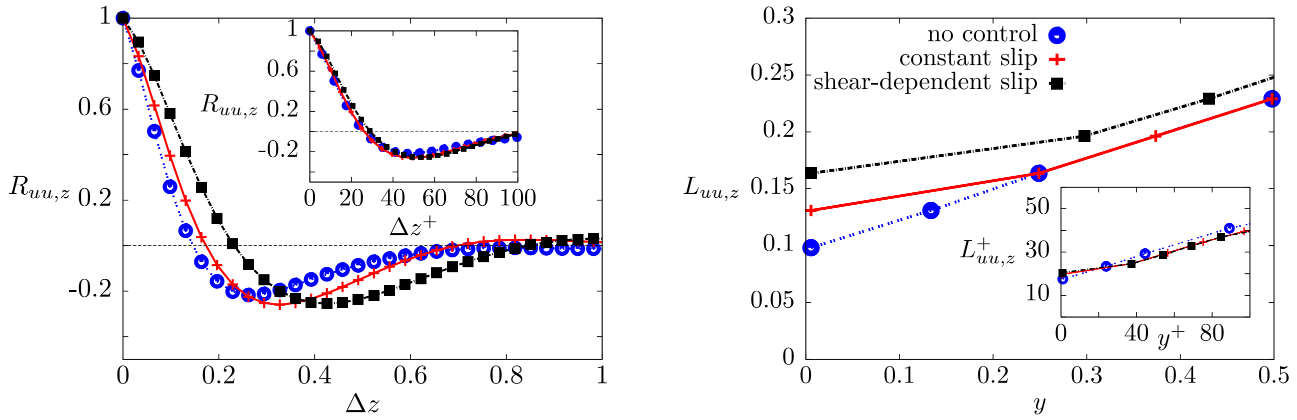

FIG. 7: Two-point spanwise correlation for the fluctuating streamwise velocity (left), defined in (54), at $y^{+0} = 12$ ($y = 0.07$) and spanwise-correlation length (right), defined in (55), as a function of y.

The spanwise correlation length $L_{uu,z}$ is computed from $R_{uu,z}$ as

$$L_{uu,z}(y) = \left\{ \min(\Delta z) \mid R_{uu}(\Delta z, y) < e^{-1} \right\} \tag{55}$$

to quantify the streak width further [9]. Figure 7 (right) shows that $L_{uu,z}$ increases with y and, for a given y, $L_{uu,z}$ attains the largest values in the shear-dependent slip-length case, especially in the near-wall region. The inset of figure 7 (right) further demonstrates that the characteristic spanwise spacing of the low-speed streaks displays a good scaling in drag-reduction viscous units.

F. Principal strain rates

To gain further insight in the physical mechanisms, we analyze the orientation of the vorticity vector $\boldsymbol{\omega}$ and the eigenvalues of the strain rate tensor $\boldsymbol{S}$, called principal strain rates and denoted by s_i, $i \in [\![1,3]\!]$. The associated eigenvectors $\boldsymbol{e}_i$ are the principal axes of the strain rate tensor. The vorticity $\boldsymbol{\omega}$ and the eigenvectors $\boldsymbol{e}_i$ define three angles θ_i that satisfy $\cos\theta_i = \boldsymbol{\omega} \cdot \boldsymbol{e}_i / (|\boldsymbol{\omega}|\, |\boldsymbol{e}_i|)$. The compressional eigendirection is $\boldsymbol{e}_3$ and the extensional one is $\boldsymbol{e}_1$ [66]. The intermediate eigenvector $\boldsymbol{e}_2$ tends to align with $\boldsymbol{\omega}$. The associated eigenvalues are ordered as $s_3 \leq s_2 \leq s_1$, with $s_1 > 0$ and $s_3 < 0$. This is the first time this approach is employed to study a drag-reduction flow.

The PDF of $\cos\theta_i$ associated with the extensional and compressional eigendirections are first computed and shown in figure 8 (left) at $y^{+0} = 10$ ($y = 0.06$). The alignment of the second eigendirection (not shown here) is not affected in the hydrophobic case. The extensional and compressional eigendirections instead show more pronounced peaks at $\cos\theta = 0$. Hydrophobic surfaces thus enhance the likelihood of the extensional and compressional eigendirection to be perpendicular to the vorticity vector. Furthermore, the extensional eigendirection from $y^{+0} = 10$ to $y^{+0} = 40$ ($y = 0.22$) present the same ratios in the PDF maximum between the uncontrolled-wall and hydrophobic cases (not shown).

The alignment of the eigendirections and $\boldsymbol{\omega}$ can be related to the turbulence dynamics. The $\boldsymbol{\omega}$ alignment with the eigendirections of the strain rate tensor S_{ij} can be interpreted by the vorticity equation:

$$\frac{D\omega_i}{Dt} = S_{ij}\omega_j + \frac{1}{R_p}\nabla^2\omega_i, \tag{56}$$

where D/Dt is the substantial derivative, S_{ij} are the components of the strain rate tensor and $\omega_i = -\epsilon_{ijk}\Omega_{jk}$ (where ϵ_{ijk} is the Levi-Civita symbol), with Ω_{jk} being the components of the rotation tensor. The first term in the right-hand-side of (56) is also found in the vortex stretching term:

$$\omega_j \frac{\partial u_i}{\partial x_j} = \omega_j S_{ij} + \omega_j \Omega_{ij}. \tag{57}$$

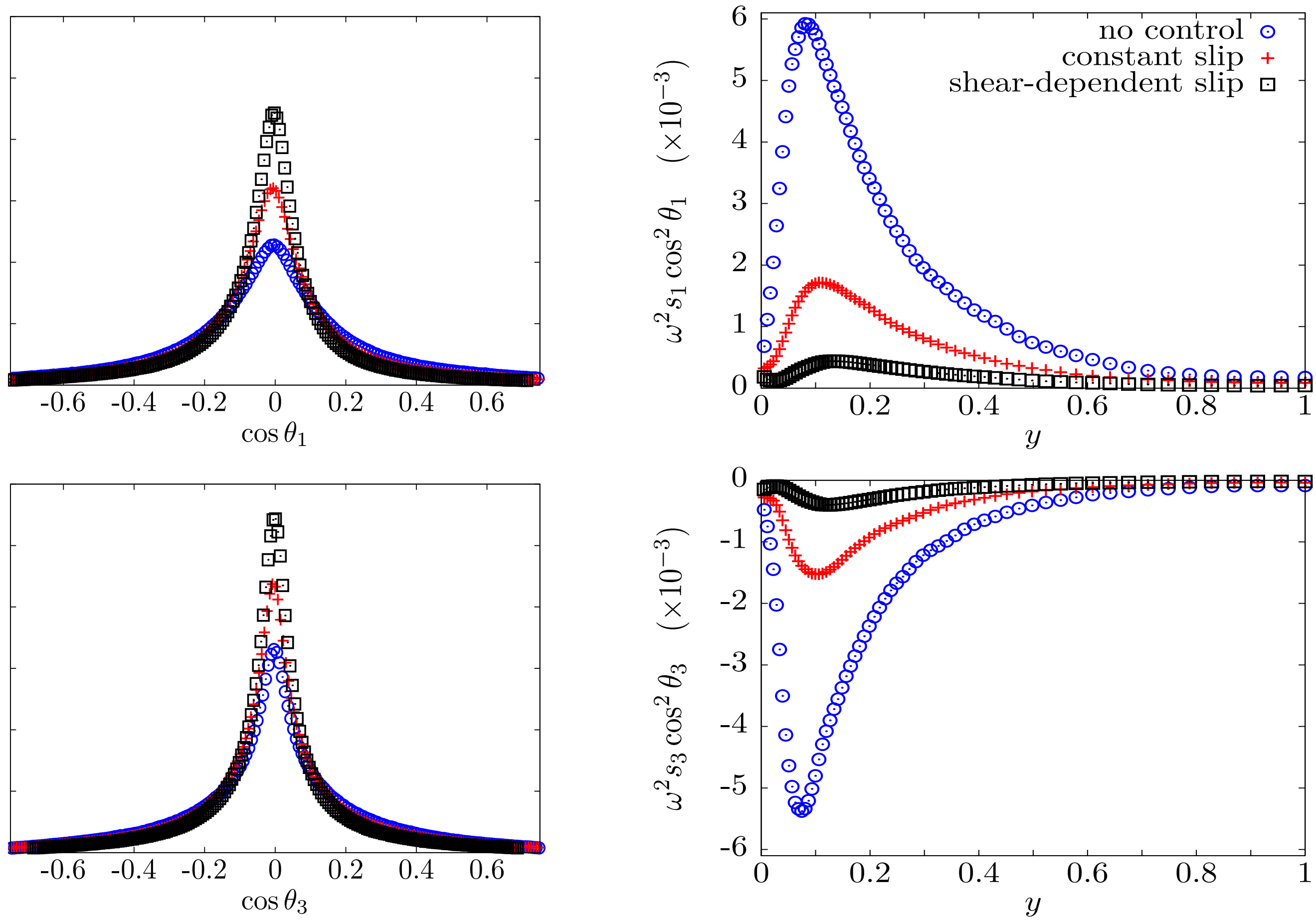

FIG. 8: Left: PDF of the extensional (top) and extensional (bottom) eigendirections. Right: contributions to the enstrophy production term given by (59) for the extensional (top) and compressional (bottom) eigendirections at $y^{+0} = 10$ ($y = 0.06$).

The second term on the right-hand-side of (57) vanishes, while the amplitude of the first term can be expressed as [66, 67]:

$$|S_{ij}\omega_j| = \omega\sqrt{s_i^2(\boldsymbol{e}_i \cdot \boldsymbol{e}_\omega)^2}, \tag{58}$$

where $\omega^2 = \omega_i\omega_i$ and $\boldsymbol{e}_\omega$ is the vorticity unit vector. It is clear from (58) that an attenuation of either the alignment term $\boldsymbol{e}_i \cdot \boldsymbol{e}_\omega$, the vorticity amplitude ω or the eigenvalues s_i contributes to a reduction of vortex stretching.

After taking the product of (56) and ω_i, the enstrophy production $\omega_i S_{ij}\omega_j$ can be linked to the quantities in (58) to explain the changes in enstrophy dynamics. The enstrophy production can be written as:

$$\omega_i S_{ij}\omega_j = \underbrace{\omega^2 s_1 \cos^2\theta_1}_{\text{I}} + \underbrace{\omega^2 s_2 \cos^2\theta_2}_{\text{II}} + \underbrace{\omega^2 s_3 \cos^2\theta_3}_{\text{III}}. \tag{59}$$

In (59) term I is always positive, term III is always negative, and II is positive in average. As shown in figure 8 (right), as terms I and III almost compensate, the main contribution to the enstrophy production is due to term II. In the hydrophobic case, $\cos\theta_1$ and $\cos\theta_3$ are strongly attenuated near the wall because the extensional and compressional eigenvectors tend to be perpendicular to the vorticity. The observation for $\boldsymbol{e}_1$ is also consistent with Buxton *et al.* [68], who mention that the perpendicular orientation of $\boldsymbol{e}_1$ with respect to $\boldsymbol{\omega}$ underlines an enstrophy

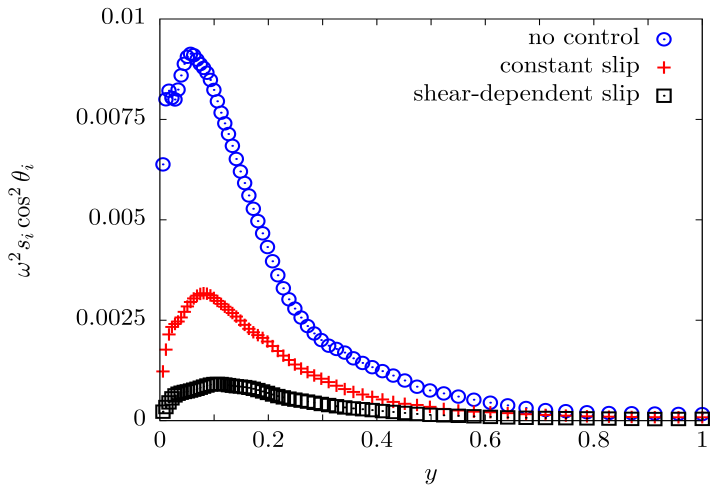

FIG. 9: Total enstrophy production rate from (59).

attenuating mechanism. Figure 9 shows that the total enstrophy production is significantly reduced compared to the uncontrolled-wall case, reflecting the attenuation of the intensity of vortical structures.

IV. SUMMARY AND OUTLOOK

In this paper laminar and turbulent channel flows with hydrophobic surfaces featuring shear-dependent slip lengths have been investigated theoretically and numerically. The slip length has been assumed to depend linearly on the wall-shear stress and therefore two constants, a and b, model the hydrophobic surface. In the turbulent flow case, the slip length is time-dependent and spatially inhomogeneous as it depends on the local instantaneous velocity gradient at the wall.

The main results are summarized in the following.

- *Laminar channel-flow solution*
  The laminar channel-flow solution with shear-dependent slip length has been derived analytically. If the shear-dependent slip length is substituted into the formula for the velocity profile, the final expression has the same form of the constant slip-length formula derived by Min and Kim [5]. The increase of mass flow rate under constant pressure gradient conditions and the decrease of wall-shear stress under constant mass flow rate conditions have been quantified. The constants a and b have been extracted from experimental data of laminar flows by Churaev *et al.* [33] and Choi and Kim [8].

- *Nonlinear Lyapunov stability analysis*
  We have carried out a three-dimensional nonlinear Lyapunov stability analysis of the channel flow between hydrophobic walls featuring a shear-dependent slip length. The stability conditions have been expressed in terms of inequalities involving the Reynolds number R_p and the constants a and b. As for a standard channel, the critical Reynolds number is very small, R_p=1/4, which is proper of microfluidic flows. Therefore, this analysis has not been useful to shed light on the mechanism of turbulent drag reduction. Nevertheless, it has been instructive to extract the stability bounds and because we have recognized that the feedback-control laws found through the analysis coincide with the slip hydrophobic-wall conditions.

- *Fukagata-Kasagi-Koumoutsakos theory*
  The theoretical formula for drag reduction prediction by Fukagata *et al.* [6] has been extended to the shear-dependent slip-length case. The computed drag reduction values show very good agreement with the direct numerical simulation results.

- *Turbulent drag reduction*
  It increases monotonically with both a and b, and also with $\mathcal{L}$, the average slip length, scaled in outer units. It

is found that flows featuring the same $\mathcal{L}$ have the same drag reduction and the same Reynolds stresses profiles, irrespectively of the values of a and b. The rms profiles of the streamwise velocity nevertheless do not overlap, demonstrating that the local behaviour of wall turbulence over these surfaces is markedly different and that the property of same $\mathcal{R}$ for same $\mathcal{L}$ is only to be considered in averaged terms. If hydrophobicity along the spanwise direction is taken into account, the drag reduction effect deteriorates. Furthermore, by rescaling our numerical slip parameters and flow conditions, we have found that even a quite weak dependence of the slip length on the wall shear can produce substantial differences in the drag-reducing properties because of the large turbulent wall shear. These a values are much smaller than the experimental ones reported by Choi and Kim [8] for a laminar flow.

- *Viscous-units scaling of near-wall statistics*
  Scaling the vorticity rms profiles with the drag-reduction friction velocity reveals that the streamwise vortices are strongly attenuated, while the low-speed streaks maintain their characteristics spacing. This is confirmed by rescaling the velocity correlations along the spanwise direction.

- *Power spent by the turbulent flow on the hydrophobic surface*
  Because of the local slip, the wall-shear stress exerts power on the hydrophobic surface, which is a non-negligible portion of the power required to propel the fluid along the streamwise direction. This shearing action is responsible for the detachment of the air bubbles from their pockets, which leads to surface degradation and the progressive loss of the drag-reducing properties. While the slip-length hydrophobic model accounts for this power expenditure, if hydrophobic surfaces are modelled as alternating patterns of no wall slip (solid boundary) and shear-free slip (air pockets), this power is null. Future research should therefore focus on the viscous effects between the turbulent liquid flow and the air pockets. For lotus-leaf-type surfaces, further analysis should focus on the precise specification of the texture geometry and of the flow motion inside the air pockets. This simulation would required coupled Navier-Stokes solvers for the liquid and gas flows with changing interface geometry to resolve fully the interaction between the turbulent liquid flow and the flow in the air pockets. Such study would clarify the influence of the liquid and gas viscosities and also reveal the role of fluctuating pressure and kinetic energy exchange at the wall. These two latter quantities also contribute to the power exchange at the wall [69] and are not modelled if the wall-normal velocity is assumed to vanish at the interface between the turbulent flow and the gas bubbles. In the turbulent regime, steps in this direction have been taken by Garcıa-Mayoral *et al.* [70], who relaxed the no-penetration condition at the wall, and by Jung *et al.* [37], who simulated a turbulent channel flow over thin air layers. Studies in the laminar regimes include Schönecker and Hardt [36] and Schönecker and Hardt [38]. Further theoretical work on the geometrical changes the liquid-gas interface due to pressure and its impact on the drag reduction properties in microfluidic flows has been carried out by Davis and Lauga [71]. In order to quantify the power spent by the liquid flow on the lotus-leaf surfaces, one idea would be to carry out an energy balance at the wall and to measure the kinetic energy of the bubbles as they detach from the surface as a consequence of the shearing and pressure action of the liquid flow. This study should include a detail analysis of the stability of the sheared air pockets.

- *Principal strain rates*
  In the hydrophobic case, the compressional and extensional eigenvectors of the strain rate tensor show a marked tendency to orient perpendicularly to the vorticity vector. This in turn causes a reduction of the vortex stretching term in the vorticity equation and an attenuation of the enstrophy production.

ACKNOWLEDGEMENTS

We acknowledge Airbus Innovation Works UK and the Department of Mechanical Engineering at the University of Sheffield for funding this work. We have used the ARCHER UK National Supercomputing Service under EPSRC Grants EP/K000225/1 and EP/L000261/1 and the computing facilities of N8 HPC funded by the N8 consortium, coordinated by the Universities of Leeds and Manchester. We would also like to thank Dr S. Laizet for his help on the use of Incompact3d, Dr M. Seddighi for his support and suggestions on the numerical method, Eva Zincone and Claudia Alvarenga for their useful comments, and Professor R.J. Poole and Drs R. Garcia-Mayoral and Y. Hasegawa for providing insightful comments on a preliminary version of the manuscript. Part of this work has been presented by SKA at the ERCOFTAC Drag Reduction and Flow Control Meeting in Cambridge, United Kingdom, in March 2015, and by PR at the "Active Drag Reduction" Symposium at RWTH Aachen in November 2015. PR acknowledges the interesting discussion with Professor S. Ceccio during the Symposium at RWTH Aachen.

Appendix A: Laminar pipe flow solution

The channel flow analysis in §II A is herein extended to the case of pipe flow. In this appendix, lengths are scaled by the pipe radius R^* and velocities by the maximum Poiseuille velocity U_p^*. The Reynolds number is defined as $R_p = U_p^* R^*/\nu^*$ and the radial direction is denoted by $r \in [0,1]$, where $r = 0$ indicates the pipe axis. In the case of fully-developed axial-symmetrical laminar pipe flow, $\mathbf{W} = (U(r), 0, 0)$, where U satisfies the simplified x-momentum,

$$\frac{1}{rR_p}\frac{\mathrm{d}}{\mathrm{d}r}\left(r\frac{\mathrm{d}U}{\mathrm{d}r}\right) - \frac{\mathrm{d}P}{\mathrm{d}x} = 0. \tag{A1}$$

The boundary conditions are

$$\begin{aligned} U(1) &= a\left(\left.\frac{\mathrm{d}U}{\mathrm{d}r}\right|_{r=1}\right)^2 - b\left.\frac{\mathrm{d}U}{\mathrm{d}r}\right|_{r=1}, \\ \left.\frac{\mathrm{d}U}{\mathrm{d}r}\right|_{r=0} &= 0. \end{aligned} \tag{A2}$$

The solution to (A1) is

$$U(r) = \frac{R_p}{4}\frac{\mathrm{d}P}{\mathrm{d}x}\left(r^2 + aR_p\frac{\mathrm{d}P}{\mathrm{d}x} - 2b - 1\right). \tag{A3}$$

The solution for $a = 0$ is also given in Watanabe *et al.* [3]. The bulk velocity is

$$\mathcal{U}_b = 2\int_0^1 U(r)r\mathrm{d}r = \frac{R_p}{8}\frac{\mathrm{d}P}{\mathrm{d}x}\left(2aR_p\frac{\mathrm{d}P}{\mathrm{d}x} - 4b - 1\right). \tag{A4}$$

Appendix B: Inequality for the time derivative of energy

In this appendix, the three terms in (19) are expanded and the condition for stability is derived. The terms in (19) are first written as:

$$\begin{aligned} 2\left[u\frac{\partial u}{\partial t}\right]_{\mathcal{I}xyz} =& -\frac{2}{R_p}\left[\frac{\partial u^2}{\partial x} + \frac{\partial u^2}{\partial y} + \frac{\partial u^2}{\partial z}\right]_{\mathcal{I}xyz} - 2\left[uv\frac{\partial \widehat{U}}{\partial y}\right]_{\mathcal{I}xyz} + 2\left[p\frac{\partial u}{\partial x}\right]_{\mathcal{I}xyz} \\ & + \frac{2}{R_p}\left[\left[u\frac{\partial u}{\partial y}\right]_0^2\right]_{\mathcal{I}xz} - \left[\left[u^2 v\right]_0^2\right]_{\mathcal{I}xz}, \end{aligned} \tag{B1}$$

$$2\left[v\frac{\partial v}{\partial t}\right]_{\mathcal{I}xyz} = -\frac{2}{R_p}\left[\frac{\partial v^2}{\partial x} + \frac{\partial v^2}{\partial y} + \frac{\partial v^2}{\partial z}\right]_{\mathcal{I}xyz} + 2\left[p\frac{\partial v}{\partial y}\right]_{\mathcal{I}xyz} + \frac{2}{R_p}\left[\left[v\frac{\partial v}{\partial y}\right]_0^2\right]_{\mathcal{I}xz}, \tag{B2}$$

$$2\left[w\frac{\partial w}{\partial t}\right]_{\mathcal{I}xyz} = -\frac{2}{R_p}\left[\frac{\partial w^2}{\partial x} + \frac{\partial w^2}{\partial y} + \frac{\partial w^2}{\partial z}\right]_{\mathcal{I}xyz} + 2\left[p\frac{\partial w}{\partial z}\right]_{\mathcal{I}xyz} + \frac{2}{R_p}\left[\left[w\frac{\partial w}{\partial y}\right]_0^2\right]_{\mathcal{I}xz}. \tag{B3}$$

The time derivative of the energy is obtained by adding the three terms in (B1), (B2), and (B3):

$$\begin{aligned} \frac{\mathrm{d}E(\mathbf{w})}{\mathrm{d}t} =& -\frac{2}{R_p}\left[\frac{\partial u^2}{\partial x} + \frac{\partial v^2}{\partial x} + \frac{\partial w^2}{\partial x} + \frac{\partial u^2}{\partial y} + \frac{\partial v^2}{\partial y} + \frac{\partial w^2}{\partial y} + \frac{\partial u^2}{\partial z} + \frac{\partial v^2}{\partial z} + \frac{\partial w^2}{\partial z}\right]_{\mathcal{I}xyz} \\ & - 2\left[uv\frac{\partial \widehat{U}}{\partial y}\right]_{\mathcal{I}xyz} + \frac{2}{R_p}\left[\left[u\frac{\partial u}{\partial y} + w\frac{\partial w}{\partial y}\right]_0^2\right]_{\mathcal{I}xz}, \end{aligned} \tag{B4}$$

where the no-penetration condition for the wall-normal velocity component, $v(x,0,z,t) = v(x,2,z,t) = 0$, has been used. Equation (B4) is employed to find an upper-bound estimate, to show global stability, and to evince how stability can be enhanced under specified conditions. The square of the streamwise velocity is written as:

$$u^2(x,y,z,t) = \left[u(x,0,z,t) + \int_0^y \frac{\partial u}{\partial y}(x,\gamma,z,t)\,\mathrm{d}\gamma \right]^2, \tag{B5}$$

and, using the inequality $(c+d)^2 \leq 2(c^2+d^2)$, the following relation is found:

$$u^2(x,y,z,t) \leq 2u^2(x,0,z,t) + 2\left[\int_0^y \frac{\partial u}{\partial y}(x,\gamma,z,t)\,\mathrm{d}\gamma \right]^2. \tag{B6}$$

Use of the Cauchy-Schwarz inequality on the second term of the right-hand-side of (B6) leads to:

$$\left[\int_0^y \frac{\partial u}{\partial y}(x,\gamma,z,t)\,\mathrm{d}\gamma \right]^2 \leq y \int_0^y \left[\frac{\partial u}{\partial y}(x,\gamma,z,t) \right]^2 \mathrm{d}\gamma. \tag{B7}$$

Combining (B6) and (B7) and integrating over the domain Ω yields:

$$\begin{aligned} \left[u^2\right]_{\mathcal{I}xyz} &\leq 2\left[u^2(x,0,z,t)\right]_{\mathcal{I}xyz} + 2\left[y \int_0^2 \frac{\partial u^2}{\partial y}(x,y,z,t)\,\mathrm{d}y \right]_{\mathcal{I}xyz} \\ &\leq 4\left[u^2(x,0,z,t)\right]_{\mathcal{I}xz} + 4\left[\frac{\partial u^2}{\partial y}\right]_{\mathcal{I}xyz}. \end{aligned} \tag{B8}$$

Analogous expressions are obtained for v and w. Adding the inequalities for the three velocity components, an upper bound on the integral of the terms involving the wall-normal derivatives in (B4) is obtained:

$$-\left[\frac{\partial u^2}{\partial y} + \frac{\partial v^2}{\partial y} + \frac{\partial w^2}{\partial y}\right]_{\mathcal{I}xyz} \leq -\frac{E(\mathbf{w})}{4} + \left[u^2(x,0,z,t) + w^2(x,0,z,t)\right]_{\mathcal{I}xz}. \tag{B9}$$

An upper bound is found for (B4):

$$\begin{aligned} \frac{\mathrm{d}E(\mathbf{w})}{\mathrm{d}t} \leq &-\frac{1}{2R_p}E(\mathbf{w}) + \frac{2}{R_p}\left[u^2(x,0,z,t) + w^2(x,0,z,t)\right]_{\mathcal{I}xz} \\ &-\frac{2}{R_p}\left[\frac{\partial u^2}{\partial x} + \frac{\partial v^2}{\partial x} + \frac{\partial w^2}{\partial x} + \frac{\partial u^2}{\partial z} + \frac{\partial v^2}{\partial z} + \frac{\partial w^2}{\partial z}\right]_{\mathcal{I}xyz} \\ &+\frac{2}{R_p}\left[\left[u\frac{\partial u}{\partial y} + w\frac{\partial w}{\partial y}\right]_0^2\right]_{\mathcal{I}xz} - 2\left[uv\frac{\partial \widehat{U}}{\partial y}\right]_{\mathcal{I}xyz}. \end{aligned} \tag{B10}$$

To find upper bounds with respect to the terms containing derivatives in x and z, the derivation is based on a Poincaré type inequality. Integrating by parts, using Young's inequality, $cd \leq \eta c^2/2 + d^2/(2\eta)$ with $\eta = 2$, and upper-bounding leads to:

$$\begin{aligned} &\int_0^{L_x} f^2(x)\,\mathrm{d}x \leq L_x f^2(L_x) + 2\int_0^{L_x} x^2 f_x^2\,\mathrm{d}x + \frac{1}{2}\int_0^{L_x} f^2(x)\,\mathrm{d}x \\ \Leftrightarrow &\int_0^{L_x} f^2(x)\,\mathrm{d}x \leq 2L_x f^2(L_x)\,\mathrm{d}x + 4\int_0^{L_x} x^2 \frac{\partial f^2}{\partial x}(x)\,\mathrm{d}x. \end{aligned} \tag{B11}$$

As $x \in [0, L_x]$, the last integral in (B11) can be further upper-bounded:

$$\int_0^{L_x} f^2(x)\,\mathrm{d}x \leq 2L_x f^2(L_x)\,\mathrm{d}x + 4L_x^2 \int_0^{L_x} \frac{\partial f^2}{\partial x}(x)\,\mathrm{d}x. \tag{B12}$$

Inequality (B12) can be applied to a function of three variables by summing over one direction at a time. For the u velocity component, these expressions are:

$$\left[u^2(x,y,z,t)\right]_{\mathcal{I}xyz} \leq 2L_x \int_0^{L_z}\int_0^{2} u^2(L_x,y,z,t)\,\mathrm{d}y\,\mathrm{d}z + 4L_x^2 \left[\frac{\partial u^2}{\partial x}\right]_{\mathcal{I}xyz}, \tag{B13}$$

$$\left[u^2(x,y,z,t)\right]_{\mathcal{I}xyz} \leq 2L_z \int_0^{L_x}\int_0^{2} u^2(x,y,L_z,t)\,\mathrm{d}y\,\mathrm{d}x + 4L_z^2 \left[\frac{\partial u^2}{\partial z}\right]_{\mathcal{I}xyz}. \tag{B14}$$

Equations (B13) and (B14) and the corresponding ones involving w lead to:

$$-\frac{2}{R_p}\left[\frac{\partial u^2}{\partial x} + \frac{\partial v^2}{\partial x} + \frac{\partial w^2}{\partial x}\right]_{\mathcal{I}xyz} \leq -\frac{E(\mathbf{w})}{2R_pL_x^2}, \tag{B15}$$

$$-\frac{2}{R_p}\left[\frac{\partial u^2}{\partial z} + \frac{\partial v^2}{\partial z} + \frac{\partial w^2}{\partial z}\right]_{\mathcal{I}xyz} \leq -\frac{E(\mathbf{w})}{2R_pL_z^2}. \tag{B16}$$

The boundedness of the equilibrium profile gives:

$$\begin{aligned} -2\left[uv\frac{\partial \widehat{U}}{\partial y}\right]_{\mathcal{I}xyz} &\leq 2\left[|u|\,|v|\right]_{\mathcal{I}xyz} \leq 2\left[u^2+v^2\right]_{\mathcal{I}xyz} \\ &\leq 2\left(E(\mathbf{w}) - \left[w^2\right]_{\mathcal{I}xyz}\right) \leq 2E(\mathbf{w}). \end{aligned} \tag{B17}$$

Substitution of (B17) into (B10) leads to

$$\begin{aligned} \frac{\mathrm{d}E(\mathbf{w})}{\mathrm{d}t} \leq &-\frac{\alpha E(\mathbf{w})}{2} + \frac{2}{R_p}\left[u^2(x,0,z,t) + w^2(x,0,z,t)\right]_{\mathcal{I}xz} \\ &+ \frac{2}{R_p}\left[\left[u\frac{\partial u}{\partial y} + w\frac{\partial w}{\partial y}\right]_0^2\right]_{\mathcal{I}xz}, \end{aligned} \tag{B18}$$

where $\alpha = {R_p}^{-1} - 4 + {R_p}^{-1}L_x^{-2} + {R_p}^{-1}L_z^{-2}$.

Appendix C: Lyapunov stability in the shear-dependent slip-length hydrophobic case

The derivation carried out in Appendix B is extended to the shear-dependent slip-length case. In the sequel, except for the final formula (C14), the dependence on x, z, t is dropped for compactness. Only the procedure for the streamwise velocity is described as the one for the spanwise velocity is analogous.

The discriminant of (24) is

$$\Delta = b^2 + 4au(y_w), \tag{C1}$$

(where $y_w = 0, 2$) which must be positive because $\partial u/\partial y \in \mathbb{R}$ and must be different from zero because otherwise $\partial u/\partial y$ would not be related to u. If $\Delta = 0$, the double root is $-b/2a$, which diverges for $a \to 0$ and $b = \mathcal{O}(1)$. The roots for the bottom wall are, $\forall a \neq 0$:

$$\frac{\partial u^{\ominus}}{\partial y}(0) = \frac{-b + \sqrt{b^2 + 4au(0)}}{2a} \, , \, \frac{\partial u^{\circledast}}{\partial y}(0) = \frac{-b - \sqrt{b^2 + 4au(0)}}{2a}, \tag{C2}$$

and the roots for the top wall are

$$\frac{\partial u^{\odot}}{\partial y}(2) = \frac{b + \sqrt{b^2 + 4au(2)}}{2a} \, , \, \frac{\partial u^{\oplus}}{\partial y}(2) = \frac{b - \sqrt{b^2 + 4au(2)}}{2a}. \tag{C3}$$

The arguments of the square-root terms must be positive. To ensure this, the amplitude of the streamwise velocity perturbation at the wall is first imposed to be bounded, $|u(0)| \leq 1$ and $|u(2)| \leq 1$. This is fully consistent with the objective of the analysis, i.e., the stabilization of the laminar flow, because $\max_y \widehat{U} = 1$. It follows that $b^2 - 4a \leq b^2 + 4au(0) \leq b^2 + 4a$ and $b^2 - 4a \leq b^2 + 4au(2) \leq b^2 + 4a$, and a sufficient condition for $b^2 + 4au(0)$ and $b^2 + 4au(2)$ to be positive is

$$a \leq b^2/4. \tag{C4}$$

The choice of the relevant roots in (C2) and (C3) is dictated by the limit $a \to 0$ with $b = \mathcal{O}(1)$, i.e., the constant-slip formulas (22) must be recovered from the shear-dependent slip-length formulas. For this purpose, (C2) and (C3) are Taylor-expanded to first order with $a \to 0$ and $b = \mathcal{O}(1)$. The Taylor expansion for $\partial u^{\ominus}/\partial y(0)$ leads to:

$$\frac{\partial u^{\ominus}}{\partial y}(0) = \frac{u(0)}{b}, \tag{C5}$$

and similarly for (C2) and (C3). The constant-slip formulas (22) are recovered as $a \to 0$, and $\partial u^{\ominus}/\partial y$ and $\partial u^{\oplus}/\partial y$ are chosen for the lower and upper wall, respectively.

The velocity gradients $\partial u^{\ominus}/\partial y$ and $\partial u^{\oplus}/\partial y$ in (C2) and (C3) and the corresponding spanwise velocity are inserted in $\mathcal{I}_{uw}$ in (20) to find:

$$\mathcal{I}_{uw} = \frac{2}{R_p}\left[u(2)\frac{\partial u^{\oplus}}{\partial y}(2) - u(0)\frac{\partial u^{\ominus}}{\partial y}(0) + w(2)\frac{\partial w^{\oplus}}{\partial y}(2) - w(0)\frac{\partial w^{\ominus}}{\partial y}(0)\right]_{\mathcal{I}xz}. \tag{C6}$$

The term containing $u^{\ominus}$ in (C6) expands as:

$$\begin{aligned} -\frac{2}{R_p}\left[u(0)\frac{\partial u^{\ominus}}{\partial y}(0)\right]_{\mathcal{I}xz} &= \frac{b}{aR_p}\left[u(0)\left(1 - \sqrt{1 + \frac{4au(0)}{b^2}}\right)\right]_{\mathcal{I}xz} \\ &= -\frac{4}{bR_p}\left[\frac{u^2(0)}{1 + \sqrt{1 + \frac{4au(0)}{b^2}}}\right]_{\mathcal{I}xz}. \end{aligned} \tag{C7}$$

The expression for the term containing $u^{\oplus}$ is analogous. Using the boundedness argument $|u(0)| \leq 1$ and $|u(2)| \leq 1$ employed in §II B, one finds

$$-\frac{4}{bR_p\left(1 + \sqrt{1 - \frac{4a}{b^2}}\right)} \leq -\frac{2}{R_p}\left[u(0)\frac{\partial u^{\ominus}}{\partial y}(0)\right]_{\mathcal{I}xz} \leq -\frac{4}{bR_p\left(1 + \sqrt{1 + \frac{4a}{b^2}}\right)}. \tag{C8}$$

Using (C8) in (C7), one finds

$$-\frac{4}{bR_p}\left[\frac{u^2(0)}{1 + \sqrt{1 + \frac{4au(0)}{b^2}}}\right]_{\mathcal{I}xz} \leq -\frac{4}{bR_p}\left[\frac{u^2(0)}{1 + \sqrt{1 + \frac{4a}{b^2}}}\right]_{\mathcal{I}xz}. \tag{C9}$$

Equations (C7) and (C9) can be used in the second integral of (C14):

$$\left[u^2(0) - u(0)\frac{\partial u^{\ominus}}{\partial y}(0)\right]_{\mathcal{I}xz} \le -\left[\frac{2}{b\left(1+\sqrt{1+\frac{4a}{b^2}}\right)} - 1\right]\left[u^2(0)\right]_{\mathcal{I}xz}. \tag{C10}$$

For the system to decay exponentially, hence achieving global stability:

$$\frac{2}{b\left(1+\sqrt{1+\frac{4a}{b^2}}\right)} \ge 1, \tag{C11}$$

i.e., $a \le 1 - b$. The derivation involving $u^{\oplus}$ is analogous,

$$\frac{2}{R_p}\left[u(2)\frac{\partial u^{\oplus}}{\partial y}(2)\right]_{\mathcal{I}xz} = \frac{b}{aR_p}\left[u(2)\left(1-\sqrt{1+\frac{4au(2)}{b^2}}\right)\right]_{\mathcal{I}xz} = -\frac{4}{bR_p}\left[\frac{u^2(2)}{1+\sqrt{1+\frac{4au(2)}{b^2}}}\right]_{\mathcal{I}xz}. \tag{C12}$$

By bounding (C12), one finds:

$$-\frac{4u^2(2)b}{R_p}\frac{1}{1+\sqrt{1-\frac{4a}{b^2}}} \le \frac{2}{R_p}u(2)\frac{\partial u^{\oplus}}{\partial y}(2) \le -\frac{4u^2(2)b}{R_p}\frac{1}{1+\sqrt{1+\frac{4a}{b^2}}}. \tag{C13}$$

The boundary term on the left-hand-side of (C13) is thus always bounded by a negative term. Substitution of (C10) and (C13) into (20) leads to:

$$\begin{aligned}\frac{\mathrm{d}E(\mathbf{w})}{\mathrm{d}t} \le &- \frac{\alpha E(\mathbf{w})}{2} - \frac{2}{R_p}\left(\frac{2}{b+\sqrt{b^2+4a}} - 1\right)\left[u^2(0)+w^2(0)\right]_{\mathcal{I}xz} \\ &- \frac{4}{R_p\left(b+\sqrt{b^2+4a}\right)}\left[u^2(2)+w^2(2)\right]_{\mathcal{I}xz}.\end{aligned} \tag{C14}$$

Expression (23) is recovered from (C14) in the limit $a \to 0$ with $b = \mathcal{O}(1)$.

Appendix D: Energy balance quantities

In this appendix, the terms of the total energy balance of the turbulent channel flow with hydrophobic walls are derived. At the wall the no-penetration condition is imposed on the wall-normal velocity component and slip is considered only along the streamwise direction. The starting point is the balance equation for the total kinetic energy (equation (1-108) in Hinze [69]):

$$\begin{aligned}\underbrace{\frac{1}{2}\frac{\partial(U_iU_i)}{\partial t}}_{\mathrm{I}} = &\underbrace{-\frac{\partial}{\partial x_j}\left[U_j\left(P+\frac{U_iU_i}{2}\right)\right]}_{\mathrm{II}} + \underbrace{\frac{1}{R_p}\frac{\partial}{\partial x_j}\left[U_i\left(\frac{\partial U_i}{\partial x_j}+\frac{\partial U_j}{\partial x_i}\right)\right]}_{\mathrm{III}} \\ &\underbrace{-\frac{1}{R_p}\left(\frac{\partial U_i}{\partial x_j}+\frac{\partial U_j}{\partial x_i}\right)\frac{\partial U_i}{\partial x_j}}_{\mathrm{IV}},\end{aligned} \tag{D1}$$

where the Einstein summation convention of repeated indices is used and all the terms are per unit mass and time. Term I is the local change of kinetic energy and term II is the change in convective transport of the pressure and kinetic energy, which is equivalent to the work done by the total dynamic pressure $P + U_iU_i/2$. Term III is the work performed by the viscous stresses and term IV is the viscous dissipation of the kinetic energy into heat. The interest is in the time average and in the volume integral of (D1). Term I vanishes through time averaging. The power $\mathcal{P}_x$ employed to pump the fluid along x is computed by time averaging and volume integration of term II, which is first written as

$$-\underbrace{\frac{1}{2}\frac{\partial\left(U_jU_iU_i\right)}{\partial x_j}}_{\text{IIa}}\underbrace{-\frac{\partial\left(U_jP\right)}{\partial x_j}}_{\text{IIb}}. \tag{D2}$$

Term IIa vanishes upon volume integration because of periodicity along x and z and because the wall-normal velocity vanishes at the walls. By introducing the time-averaged quantities and by integrating along x, the power $\mathcal{P}_x$ is

$$\mathcal{P}_x = -\left[\overline{\frac{\partial\left(U_jP\right)}{\partial x_j}}\right]_{\mathcal{I}xyz} = \int_0^2\int_0^{L_z}\left[\left(\overline{U}\ \overline{P}\right)\big|_{x=0} - \left(\overline{U}\ \overline{P}\right)\big|_{x=L_x}\right]\mathrm{d}z\mathrm{d}y, \tag{D3}$$

where use has been made of the periodicity along z and of the no-penetration condition at the walls. Due to the time-averaged pressure being independent of y and z and to the periodicity of the velocity along x, it is found

$$\mathcal{P}_x = 2L_z\mathcal{U}_b\left(\overline{P}\big|_{x=0} - \overline{P}\big|_{x=L_x}\right) = 2\mathcal{U}_bL_xL_z\left(\frac{R_\tau}{R_p}\right)^2. \tag{D4}$$

Use has been made of (33), (34), and the time- and space-averaged x-momentum equation at the walls.

The volume integral of time-averaged term III is the work $\mathcal{W}$ done by the fluid on the surface through the viscous stresses:

$$\mathcal{W} = \frac{1}{R_p}\left[\overline{\frac{\partial}{\partial x_j}\left[U_i\left(\frac{\partial U_i}{\partial x_j}+\frac{\partial U_j}{\partial x_i}\right)\right]}\right]_{\mathcal{I}xyz} = -\frac{2}{R_p}\left[\overline{U(0)\left.\frac{\partial U}{\partial y}\right|_{y=0}}\right]_{\mathcal{I}xz}. \tag{D5}$$

The final expression is obtained by using the periodicity along x and z and the no-penetration condition at the walls for the wall-normal velocity component.

The volume integral of time-averaged term IV is the total viscous dissipation of kinetic energy into heat:

$$\mathcal{D} = -\frac{1}{R_p}\left[\overline{\left(\frac{\partial U_i}{\partial x_j}+\frac{\partial U_j}{\partial x_i}\right)\frac{\partial U_i}{\partial x_j}}\right]_{\mathcal{I}xyz}. \tag{D6}$$

The volume integral of the time-averaged kinetic energy equation (D1) is therefore:

$$\mathcal{P}_x + \mathcal{W} + \mathcal{D} = 0. \tag{D7}$$

In the case of uncontrolled walls, (D7) reduces to

$$\mathcal{P}_{x,r} + \mathcal{D}_r = 0. \tag{D8}$$

By dividing each term of (D7) by $\mathcal{P}_{x,r}$, one finds:

$$100 - \mathcal{R} + \mathcal{P}_{sp} + \frac{100\mathcal{D}}{\mathcal{P}_{x,r}} = 0, \tag{D9}$$

where the percent power spent is $\mathcal{P}_{sp}(\%) = 100\mathcal{W}/\mathcal{P}_{x,r}$. The drag reduction $\mathcal{R}$ appears in (D9) by use of (31), (32), (33), and (34).

Appendix E: Average of the wall-normal velocity gradient and definition of average slip length

In this appendix the error in assuming that (41) is valid is quantified. Expression (41) is found by first space- and time-averaging (1). As in the constant-slip-length case studied by FKK, the second term on the right-hand-side of (41) is obtained directly because the order of the integral operators used in (29) and the wall-normal derivative operator can be switched. By applying the space- and time-averaging operators (21) and (30) to the first term on the right-hand-side (1), one finds:

$$\mathcal{A} = \frac{1}{L_x L_z} \left[\overline{\left(\left. \frac{\partial U}{\partial y} \right|_{y=0} \right)^2} \right]_{\mathcal{I}xz} . \tag{E1}$$

In order to express (E1) as a function of the mean velocity $\mathcal{U}$, the square of the mean-flow wall-normal gradient is instead considered:

$$\mathcal{B} = \left[\frac{1}{L_x L_z} \left[\overline{\left. \frac{\partial U}{\partial y} \right|_{y=0}} \right]_{\mathcal{I}xz} \right]^2 = \left(\left. \frac{\mathrm{d}\mathcal{U}}{\mathrm{d}y} \right|_{y=0} \right)^2 = \frac{C_f^2 R_p^2 \mathcal{U}_b^4}{4} . \tag{E2}$$

The last two in (E2) follow from (29) and (31). The percent relative error $\mathcal{E}$ between $\mathcal{A}$ and its approximation $\mathcal{B}$ is:

$$\mathcal{E}(\%) = 100 \times \left| \frac{\mathcal{A} - \mathcal{B}}{\mathcal{A}} \right| . \tag{E3}$$

The error $\mathcal{E}$ is less than 1%.

Along the same lines, two definitions of the average slip length are proposed. It can be be defined as

$$\mathcal{L}_1 = (L_x L_z)^{-1} \left[\overline{l_s} \right]_{\mathcal{I}xz} , \tag{E4}$$

where $l_s(x, z, t)$ is defined in (1), or as

$$\mathcal{U}(0) = \mathcal{L}_2 \left. \frac{\mathrm{d}\mathcal{U}}{\mathrm{d}y} \right|_{y=0} . \tag{E5}$$

As the two lengths show very good agreement, the average slip length is indicated by $\mathcal{L}$.

---

[1] M. Gad-el Hak, *Flow control - Passive, Active and Reactive Flow Management* (Cambridge University Press, 2000).
[2] J.R. Philip, "Flows satisfying mixed no-slip and no-shear conditions," Z. Angew. Math. und Phys. **23**, 353–372 (1972).
[3] K. Watanabe, Y. Udagawa, and H. Udagawa, "Drag reduction of Newtonian fluid in a circular pipe with a highly water-repellent wall," J. Fluid Mech. **381**, 225–238 (1999).
[4] T. Min and J. Kim, "Effects of hydrophobic surface on skin-friction drag," Phys. Fluids **16** (2004).
[5] T. Min and J. Kim, "Effects of hydrophobic surface on stability and transition," Phys. Fluids **17** (2005).
[6] K. Fukagata, N. Kasagi, and P. Koumoutsakos, "A theoretical prediction of friction drag reduction in turbulent flow by superhydrophobic surfaces," Phys. Fluids **18**, 051703 (2006).
[7] E. Lauga and H.A. Stone, "Effective slip in pressure-driven Stokes flow," J. Fluid Mech. **489**, 55–77 (2003).
[8] C.H. Choi and C.J. Kim, "Large slip of aqueous liquid flow over a nanoengineered superhydrophobic surface," Phys. Rev. Lett. **96** (2006).
[9] A. Busse and N. D. Sandham, "Influence of an anisotropic slip-length boundary condition on turbulent channel flow," Phys. Fluids **24**, 055111 (2012).
[10] L. Feng, S. Li, Y. Li, H. Li, L. Zhang, J. Zhai, Y. Song, B. Liu, L. Jiang, and D. Zhu, "Super-hydrophobic surfaces: from natural to artificial," Advanced Materials **14**, 1857–1860 (2002).
[11] T.-S. Wong, S.H. Kang, S.K.Y. Tang, E.J. Smythe, B.D. Hatton, A. Grinthal, and J. Aizenberg, "Bioinspired self-repairing slippery surfaces with pressure-stable omniphobicity," Nature **477**, 443–447 (2011).
[12] P.W. Wilson, W. Lu, H. Xu, P. Kim, M.J. Kreder, J. Alvarenga, and J. Aizenberg, "Inhibition of ice nucleation by slippery liquid-infused porous surfaces (slips)," Phys. Chemistry Chem. Phys. **15**, 581–585 (2013).
[13] J.S. Wexler, I. Jacobi, and H.A. Stone, "Shear-driven failure of liquid-infused surfaces," Phys. Rev. Letters **114**, 168301 (2015).
[14] I. Jacobi, J.S. Wexler, and H.A. Stone, "Overflow cascades in liquid-infused substrates," Phys. Fluids **27**, 082101 (2015).
[15] B.J. Rosenberg, T. Van Buren, M.K. Fu, and A.J. Smits, "Turbulent drag reduction over air-and liquid-impregnated surfaces," Phys. Fluids **28**, 015103 (2016).
[16] J. Ou and J.P. Rothstein, "Direct velocity measurements of the flow past drag-reducing ultrahydrophobic surfaces," Phys. Fluids **17**, 103606–103606 (2005).
[17] A. Busse, N.D. Sandham, G. McHale, and M.I. Newton, "Change in drag, apparent slip and optimum air layer thickness for laminar flow over an idealised superhydrophobic surface," J. Fluid Mech. **727**, 488–508 (2013).
[18] J. Ou, B. Perot, and J.P. Rothstein, "Laminar drag reduction in microchannels using ultrahydrophobic surfaces," Phys.

Fluids **16**, 4635–4643 (2004).

[19] C.L.M.H. Navier, "Mémoire sur les lois du mouvement des fluides," Mémoires de l'Académie Royale des Sciences de l'Institut de France (1823).

[20] R.J. Daniello, N.E. Waterhouse, and J.P. Rothstein, "Drag reduction in turbulent flows over superhydrophobic surfaces," Phys. Fluids **21** (2009).

[21] E. Aljallis, M.A. Sarshar, R. Datla, V. Sikka, A. Jones, and C.-H. Choi, "Experimental study of skin friction drag reduction on superhydrophobic flat plates in high reynolds number boundary layer flow," Phys. Fluids **25**, 025103 (2013).

[22] R. A. Bidkar, L. Leblanc, A. J. Kulkarni, V. Bahadur, S. L. Ceccio, and M. Perlin, "Skin-friction drag reduction in the turbulent regime using random-textured hydrophobic surfaces," Phys. Fluids (1994-present) **26**, 085108 (2014).

[23] Y. Hasegawa, B. Frohnapfel, and N. Kasagi, "Effects of spatially varying slip length on friction drag reduction in wall turbulence," in *J. Phys.: Conf. Series*, Vol. 318 (IOP Publ., 2011) p. 022028.

[24] A.D. Stroock, S.K. Dertinger, G.M. Whitesides, and A. Ajdari, "Patterning flows using grooved surfaces," Analytical Chemistry **74**, 5306–5312 (2002).

[25] M.Z. Bazant and O.I. Vinogradova, "Tensorial hydrodynamic slip," J. Fluid Mech. **613**, 125–134 (2008).

[26] M.B. Martell, J.B. Perot, and J.P. Rothstein, "Direct numerical simulations of turbulent flows over superhydrophobic surfaces," J. Fluid Mech. **620**, 31–41 (2009).

[27] M.B. Martell, J.P. Rothstein, and J.B. Perot, "An analysis of superhydrophobic turbulent drag reduction mechanisms using direct numerical simulation," Phys. Fluids **22**, 065102 (2010).

[28] J. Lee, T.O. Jelly, and T.A. Zaki, "Effect of Reynolds number on turbulent drag reduction by superhydrophobic surface textures," Flow, Turbulence and Combustion **95**, 277–300 (2015).

[29] J.P. Rothstein, "Slip on superhydrophobic surfaces," Ann. Rev. Fluid Mech. **42**, 89–109 (2010).

[30] T.O. Jelly, S.Y. Jung, and T.A. Zaki, "Turbulence and skin friction modification in channel flow with streamwise-aligned superhydrophobic surface texture," Phys. Fluids **26**, 095102 (2014).

[31] E. Bonaccurso, H-J. Butt, and V.S.J. Craig, "Surface roughness and hydrodynamic boundary slip of a Newtonian fluid in a completely wetting system," Phys. Rev. Lett. **90**, 144501 (2003).

[32] C.-H. Choi, K.J.A. Westin, and K.S. Breuer, "Apparent slip flows in hydrophilic and hydrophobic microchannels," Phys. Fluids **15**, 2897 (2003).

[33] N.V. Churaev, V.D. Sobolev, and A.N. Somov, "Slippage of liquids over lyophobic solid surfaces," J. Coll. Int. Sci. **97**, 574–581 (1984).

[34] V.S.J. Craig, C. Neto, and D.R.M. Williams, "Shear-dependent boundary slip in an aqueous Newtonian liquid," Phys. Rev. Lett. **87**, 054504 (2001).

[35] C. Schönecker, T. Baier, and S. Hardt, "Influence of the enclosed fluid on the flow over a microstructured surface in the Cassie state," J. Fluid Mech. **740**, 168–195 (2014).

[36] C. Schönecker and S. Hardt, "Longitudinal and transverse flow over a cavity containing a second immiscible fluid," J. Fluid Mech. **717**, 376–394 (2013).

[37] T. Jung, H. Choi, and J. Kim, "Effects of the air layer of an idealized superhydrophobic surface on the slip length and skin-friction drag," J. Fluid Mech. **790**, R1 (2016).

[38] C. Schönecker and S. Hardt, "Assessment of drag reduction at slippery, topographically structured surfaces," Microfluidics and Nanofluidics. , 1–9 (2015).

[39] S. Laizet and E. Lamballais, "High-order compact schemes for incompressible flows: A simple and efficient method with quasi-spectral accuracy," J. Comp. Phys. **228**, 5989–6015 (2009).

[40] S. Laizet and N. Li, "Incompact3d: A powerful tool to tackle turbulence problems with up to $\mathcal{O}(10^5)$ computational cores," Int. J. Num. Meth. Fluids **67**, 1735–1757 (2011).

[41] A. Balogh, W.J. Liu, and M. Krstic, "Stability enhancement by boundary control in 2-D channel flow," IEEE Trans. Aut. Control **46**, 1696–1711 (2001).

[42] P.A. Thompson and S.M. Troian, "A general boundary condition for liquid flow at solid surfaces," Nature **389**, 360–362 (1997).

[43] A. Balogh, O.M. Aamo, and M. Krstic, "Optimal mixing enhancement in 3-d pipe flow," IEEE Trans. Control Syst. Tech. **13**, 27–41 (2005).

[44] A.V. Fedorov and A. P. Khokhlov, "Prehistory of instability in a hypersonic boundary layer," Th. Comp. Fluid Dyn. **14**, 359–375 (2001).

[45] A. Fedorov, A. Shiplyuk, A. Maslov, E. Burov, and N. Malmuth, "Stabilization of a hypersonic boundary layer using an ultrasonically absorptive coating," J. Fluid Mech. **479**, 99–124 (2003).

[46] A.N. Shiplyuk, E. V. Burov, A.A. Maslov, and V. M. Fomin, "Effect of porous coatings on stability of hypersonic boundary layers," J. Applied Mech. Tech. Phys. **45**, 286–291 (2004).

[47] J. Jiménez, M. Uhlmann, A. Pinelli, and G. Kawahara, "Turbulent shear flow over active and passive porous surfaces," J. Fluid Mech. **442**, 89–117 (2001).

[48] P. Ricco and S. Hahn, "Turbulent drag reduction through rotating discs," J. Fluid Mech. **722**, 267–290 (2013).

[49] R. B. Dean, "Reynolds number dependence of the skin friction and other bulk flow variables in two-dimensional rectangular duct flow," J. Fluids Eng. **100**, 215–223 (1978).

[50] S. Hoyas and J. Jiménez, "Scaling of the velocity fluctuations in turbulent channels up to Re_τ=2003," Phys. Fluids **18**, 011702 (2006).

[51] I. Marusic, B.J. McKeon, P.A. Monkewitz, H.M. Nagib, A.J. Smits, and K.R. Sreenivasan, "Wall-bounded turbulent flows at high Reynolds numbers: Recent advances and key issues," Phys. Fluids **22** (2010).

[52] M. Bernardini, S. Pirozzoli, and P. Orlandi, “Velocity statistics in turbulent channel flow up to $Re_\tau = 4,000$,” J. Fluid Mech. **742**, 171–191 (2014).
[53] W.L. Dunn and J.K. Shultis, *Exploring Monte Carlo methods* (Elsevier, 2011).
[54] K. Fukagata, K. Iwamoto, and N. Kasagi, “Contribution of Reynolds stress distribution to the skin friction in wall-bounded flows,” Phys. Fluids **14**, 73–76 (2002).
[55] S.B. Pope, *Turbulent Flows* (Cambridge University Press, 2000).
[56] R.N. Govardhan, G.S. Srinivas, A. Asthana, and M.S. Bobji, “Time dependence of effective slip on textured hydrophobic surfaces,” Phys. Fluids **21**, 052001 (2009).
[57] W.J. Jung, N. Mangiavacchi, and R. Akhavan, “Suppression of turbulence in wall-bounded flows by high-frequency spanwise oscillations,” Phys. Fluids A **4**, 1605–1607 (1992).
[58] M. Quadrio and P. Ricco, “The laminar generalized Stokes layer and turbulent drag reduction,” J. Fluid Mech. **667**, 135–157 (2011).
[59] D. Roggenkamp, W. Jessen, W. Li, M. Klaas, and W. Schröder, “Experimental investigation of turbulent boundary layers over transversal moving surfaces,” CEAS Aeron. J. , 1–14 (2015).
[60] J. Kim, P. Moin, and R. Moser, “Turbulence statistics in fully developed channel flow at low Reynolds number,” J. Fluid Mech. **177**, 133–166 (1987).
[61] H. Choi, P. Moin, and J. Kim, “Active turbulence control for drag reduction in wall-bounded flows,” J. Fluid Mech. **262**, 75–110 (1994).
[62] J. Jiménez, “On the structure and control of near wall turbulence,” Phys. Fluids **6**, 944 (1994).
[63] A.G. Kravchenko, H. Choi, and P. Moin, “On the relation of near-wall streamwise vortices to wall skin friction in turbulent boundary layers,” Phys. Fluids **5**, 3307–3309 (1993).
[64] S.J. Kline, W.C. Reynolds, F.A. Schraub, and P.W. Runstadler, “The structure of turbulent boundary layers,” J. Fluid Mech. **30**, 741 (1967).
[65] R.L. Panton, “Overview of the self-sustaining mechanisms of wall turbulence,” Progr. Aero. Sc. **37**, 341–383 (2001).
[66] P.E. Hamlington, J. Schumacher, and W.J.A. Dahm, “Direct assessment of vorticity alignment with local and nonlocal strain rates in turbulent flows,” Phys. Fluids **20**, 111703 (2008).
[67] R. Betchov, “An inequality concerning the production of vorticity in isotropic turbulence,” J. Fluid Mech. **1**, 497–504 (1956).
[68] O.R.H. Buxton, S. Laizet, and B. Ganapathisubramani, “The interaction between strain-rate and rotation in shear flow turbulence from inertial range to dissipative length scales,” Phys. Fluids **23**, 061704 (2011).
[69] J.O. Hinze, *Turbulence* (McGraw Hill, Inc. – Second Edition, 1975).
[70] R. Garcıa-Mayoral, J. Seo, and A. Mani, “Dynamics of gas-liquid interfaces in turbulent flows over superhydrophobic surfaces,” in *Proc. CTR Summer Program* (2014) p. 295.
[71] A.M.J. Davis and E. Lauga, “Geometric transition in friction for flow over a bubble mattress,” Phys. Fluids **21**, 011701 (2009).